LA-UR- 09-00756

Approved for public release;
distribution is unlimited.

Title:	Modeling of the Phase Evolution in Mg1-xAlxB2 (0 < x < 0.5) and its Experimental Signatures
Author(s):	D. A. Andersson, L. Casillas, J. Lezama and S. D. Conradson
Intended for:	Publication in Journal of Physical Chemistry B

Los Alamos
NATIONAL LABORATORY
EST. 1943

Form 836 (7/06)

Modeling of the Phase Evolution in $Mg_{1-x}Al_xB_2$ ($0 < x < 0.5$) and its Experimental Signatures

David A. Andersson, Luis Casillas, Juan Lezama, and Steven D. Conradson

Materials Science and Technology Division, Los Alamos National Laboratory, Los Alamos, NM 87545, USA

andersson@lanl.gov

RECEIVED DATE

CORRESPONDING AUTHOR FOOTNOTE

Despite the chemical and structural simplicity of MgB_2, at 39 K this compound has the highest known T_c of any binary compound. Electron doping by substituting Al for Mg leads to decreasing T_c and the observed concentration dependent rate of decrease has been proposed to arise from the non-ideal character of MgB_2-AlB_2 solid solutions, which derives from the existence of an ordered $Mg_{0.5}Al_{0.5}B_2$ compound. Heterogeneous nano-scale structure patterns in solid solutions have emerged as an important concept for complex materials, ranging from actinide alloys and oxides to high-temperature cuprate superconductors and manganite-based materials exhibiting colossal magnetoresistivity. In this work we investigate the formation of structural heterogeneities in $Mg_{1-x}Al_xB_2$, which take the form of nano-scale Al-Al and Al-Mg domains of different geometry and size, using molecular statics/dynamics simulations and in particular we study the corresponding signatures in diffraction experiments. In order to undertake this task we first derive appropriate

Mg-Al-B semi-empirical potentials within the Modified Embedded Atom Method formalism. These potentials are also applied to explore the equilibrium $Mg_{1-x}Al_xB_2$ phase diagram for $0 < x < 0.5$. Additionally, density functional theory calculations were utilized to study the influence of heterogeneities on the electronic structure and charge distribution in $Mg_{1-x}Al_xB_2$.

KEYWORDS

Introduction

With a superconducting transition temperature (T_c) of 39 K,[1] MgB_2 has the highest T_c of any binary compound,[1,2] and the pairing mechanism is believed to be of BCS-like origin.[3,4,5,6,7,8,9,10] The simple hexagonal AlB_2-type crystal structure of MgB_2, in which graphite-like layers of B atoms are separated by hexagonal metal planes that occupy positions above/below the empty holes of the B layers, made this discovery even more intriguing and altogether this sparked intense research activities, trying to explain these features and to further raise T_c by, for example, various chemical alterations.[3,11,12,13,14] One approach involved partial substitution of Mg by Al (AlB_2 is isostructural to MgB_2), which effectively results in electron doping due to the difference in preferred valence between Mg^{2+} and Al^{3+} ions.[11] Unfortunately, all attempts resulted in decreasing T_c and in the case of Al substitution this was explained by the fact that electron doping fills additional electronic states and as a consequence the density of states at the Fermi level decreases, thus lowering T_c according to BCS theory.[3,11,15] The rate of decrease of T_c is a function of the Al content (x_{Al});[3,11] T_c first decreases at a constant rate for $0<x<0.10$, after which there is a slightly scattered, but still decreasing, distribution of T_c up to $x_{Al}\approx0.25$ and from 0.25 to 0.40 there is a significant fall-off and beyond $x_{Al}=0.60$ superconductivity disappears completely.[3,11,16,17,18] This behavior has been shown to correlate with the appearance of a second ordered phase of the $Mg_{0.5}Al_{0.5}B_2$ composition for $x_{Al} > 0.10$.[3,11,18,19] This phase is composed of an alternating stacking sequence of pure Al and Mg planes along the c-axis.[3,18] For $0.1<x<0.25$ there is a miscibility gap that involves $Mg_{1-x}Al_xB_2$ and a non-stoichiometric form of the ordered $Mg_{0.5}Al_{0.5}B_2$ phase, $Mg_{0.5+y}Al_{0.5-y}B_2$.[18]

For x>0.25 there is a single $Mg_{0.5+y}Al_{0.5-y}B_2$ phase field.[18] Reaching beyond MgB_2-AlB_2, nano-scale heterogeneities that are either at or below the diffraction limit in size have emerged as an important concept for high-T_c cuprate superconductors,[20,21,22,23,24] manganite-based materials exhibiting colossal magnetoresistivity[25,26] (CMR) and also for actinide compounds and alloys, e.g. PuO_{2+x}/UO_{2+x}[27,28] and $Pu_{1-x}Ga_x$.[29] Howell *et al.*,[30] Garcia-Adeva *et al.*[31] and Espinosa-Faller *et al.*[32] have extensively studied how nano-scale L_{10} domains within a disordered fcc matrix may be invisible for diffraction techniques, while still giving rise to distinct physical properties, as for example signatures of anti-ferromagnetic ordering in presumably paramagnetic NiMn random alloys. These anti-ferromagnetic properties were proposed to originate from nano-scale L_{10} NiMn domains, which thus share the properties of the anti-ferromagnetic L_{10} NiMn bulk phase, within the disordered fcc phase. Since the L_{10} NiMn domains are below the diffraction limit in size, the bulk L_{10} character is not revealed by diffraction techniques and instead the material appears to be a random solid solution from a structural point of view.[31,32] Howell *et al.* explored the conditions on the L_{10} domain size and on the strain relaxation between L_{10} and fcc phase components for the appearance of L_{10} diffraction signatures.[30] This study was performed by projecting the three-dimensional fcc lattice onto a two-dimensional Hamiltonian. The present work on $Mg_{1-x}Al_xB_2$ extends the studies on closed packed alloys[30,31,32] to systems exhibiting more complex open crystal structures and, unlike the two-dimensional projections applied in Ref. 30, we provide a full three-dimensional treatment of the $Mg_{1-x}Al_xB_2$ system. One of the prerequisites for the formation of nano-sized heterogeneities is being in the proximity of a phase transition, diffusion-assisted as in $UO_{2+x}/PuO_{2+x}/Mg_{1-x}Al_xB_2$[3,11,27,28] or diffusion-less (martensitic), e.g. driven by electronic/magnetic/charge ordering, as in high-T_c cuprates and CMR manganites,[20,21,22,23,24,25,26] the reason being that there must be two competing structure/ordering patterns available for the atomic constituents; at the same time growth into macroscopic phase components is hindered due to either kinetic or energetic restrictions. For the nano-scale domains of diffusion-less origin, the smallest length-scale is set by the martensites linked to the majority or host lattice structure. In the present study of $Mg_{1-x}Al_xB_2$ we address some of the

thermodynamic issues related formation of nano-scale heterogeneities that were principally neglected in the earlier works on L_{10} ordering within disordered fcc lattices.[30]

$Mg_{1-x}Al_xB_2$ is used as a test/model system for the concept of nano-scale heterogeneities, which, presumably, is much simpler than the complex oxide systems that were mentioned in the previous paragraph and thus a more convenient starting point. We study the emergence of nano-scale domains of various geometry, size and composition within the MgB_2 matrix. In particular, we are interested in how such non-periodic structure patterns are distinguished by diffraction techniques, which inherently rely on averaging of the lattice to capture the periodic component of the structure and thus should have limited ability to identify aperiodic nano-scale patterns, at least as long as they are below the diffraction limit in size. We address both the thermodynamically most stable $Mg_{1-x}Al_xB_2$ structure patterns as well as a number of metastable patterns. The various $Mg_{1-x}Al_xB_2$ structures are relaxed using molecular statics and from the relaxed structures we simulate the (powder) diffraction patterns to identify any specific features that derive from the nano-scale domains and/or the lattice strain that they induce. In order to evaluate structural and thermodynamic properties of $Mg_{1-x}Al_xB_2$ we have derived appropriate MEAM (Modified Embedded Atom Method) semi-empirical potentials from density functional theory calculations and available experimental data.

Our paper is organized as follows. First we describe the methodology, which includes specifying the MEAM potentials and a brief review of the formalism applied to calculate the diffraction patterns. In the next section we present results from the density functional theory calculations on MgB_2, AlB_2 and $Mg_{0.5}Al_{0.5}B_2$ compounds. After this we discuss the MgB_2-AlB_2 thermodynamics and the diffraction signatures from ordered compounds as well as from $Mg_{1-x}Al_xB_2$ solid solutions exhibiting nano-scale heterogeneities. The electronic structure of MgB_2, AlB_2 and $Mg_{1-x}Al_xB_2$ compounds is studied in the final section.

Methodology

The MgB_2 crystal structure consists of graphite-like layers of B atoms separated by hexagonal metal planes that occupy positions above/below the empty holes of the B layers. Strong covalent B-B bonds with significant directional character hold the B planes together. The weakly metallic interplanar Mg-B bonds are stronger than the Mg-Mg intraplanar bonds, which exhibit a dominating ionic character.[33] AlB_2 is iso-structural to MgB_2 and possesses similar bonding properties. The Modified Embedded Atom Model (MEAM)[34,35,36,37,38,39,40] type of semi-empirical potentials should be suitable for describing the particular bonding characteristics of the MgB_2-AlB_2 system, including the directional B-B bonds, and this formalism is consequently applied to parameterize the potential energy surface of the $Mg_{1-x}Al_xB_2$ system. The energy in the MEAM formalism is expressed as[37,38,39,40];

$$E=\Sigma(F_i(\rho_i/Z_i)+1/2\Sigma\phi_{ij}(R_{ij}))$$

Here, F_i is the embedding function for atom i in a background electron density ρ_i, Z_i is the number of first nearest neighbors of atom i in its references structure, ϕ_{ij} is the pair potential between atoms i and j, and R_{ij} represents the corresponding atomic separation. The pair potential, ϕ_{ij}, applies the functional form proposed by Rose *et al.*,[41] which is parameterized by the nearest neighbor distance (r_e), the atomic volume (Ω), the bulk modulus (B) and the cohesive energy (E_c). The embedding function, F_i, applies the functional form specified in Ref. 40 and the background electron densities, ρ_i, are obtained from an expansion of the partial electron densities for each atom type, modulated by an exponential radial decay. The detailed ρ_i expansions are specified in Ref. 40,42 and applies two sets of parameters; the $t^{(k)}$ parameters (k=0, 1, 2 and 3) are the expansion coefficients for the partial electron densities for each atom type, ρ_0 is a scaling factor applied to the partial densities,[37,38,39,40,42] and the $\beta^{(k)}$ (k=0, 1, 2 and 3) parameters describe the exponential decay of the respective partial charge densities.[37,38,39,40,42] MEAM potentials for elemental Mg and Al have been published by Jelinek *et al.*,[43] though, in order to optimize the description of the current B-containing systems, slight modifications, as specified below, were

introduced to these potentials. Unlike Mg and Al, there is no published MEAM B potential, and an unpublished version partially predicted anomalous shear instabilities for both MgB_2 and AlB_2. Consequently, we have derived a new MEAM B potential to be used in this study. The elemental Mg, Al and B MEAM parameters are summarized in Table 1 and the Mg-Al-B cross terms are specified in Table 2 and Table 3. The derivation of these parameters is further discussed in the Results/Discussion section. Table 2 and Table 3 contain two different parameter sets for the Mg-Al-B cross terms, which is a requirement that arise from difficulties of describing the complete thermodynamic and structural MgB_2-AlB_2 information within a single MEAM parameterization (the so-called non-thermodynamic consistent [NTC] set in Table 2) without introducing special rules for the screening between Al and Mg atoms, as was done for the parameter set in Table 3 (the so-called thermodynamic consistent set [TC]). The screening parameters, C(i,j,k), specify how the i-j atom pair is screened by atom k, and the functional form of the screening function is for example defined in Refs. 39,43. Table 4 (NTC) and Table 5 (TC) collect the screening parameters for the two Mg-Al-B MEAM parameter sets.

Elem	Lat	α	β_0	β_1	β_2	β_3	a_{lat}	E_c	r_e	t_0	t_1	t_2	t_3	ρ_0
Mg	hcp	5.45	2.70	0.00	0.35	3.00	3.20	1.55	1.11	1.00	8.00	4.10	-2.00	0.60
Al	fcc	4.64	2.04	1.50	6.00	1.50	4.05	3.353	1.07	1.00	4.00	-2.30	8.01	1.00
B	dia	3.90	2.80	6.00	1.00	1.30	4.043	5.49	0.80	1.00	1.00	0.40	-0.20	2.00

Table 1: The elemental Mg, Al and B MEAM parameter sets used in the present work. 'Lat' stands for reference lattice and 'Elem' for the element in question. The t_i variables are the expansion coefficient for the partial electron densities and ρ_0 is a scaling factor applied to the partial densities.[37,38,39,40,42] The β_i parameters describe the exponential decay of the respective partial charge densities.[37,38,39,40,42] The α parameter is defined by $\alpha^2=9\Omega B/E_c$, where Ω is the atomic volume, B is the bulk modulus and E_c is the cohesive energy. The r_e and a_{lat} parameters represent the equilibrium distance between atoms and the lattice constant of the reference lattice, respectively. The scaling factors for the embedding energies are all set to 1.

	E_c	Ref	r_c	α	r_e	ρ_0
Al-Mg	-0.32	B1	5.0	4.17	2.821	1.0,0.6
Mg-B	0.33	B1	4.0	4.00	2.478	0.6,7.0
Al-B	0.22	B1	4.0	4.00	2.3015	1.1,7.0

Table 2: The non-thermodynamic consistent Mg-Al-B parameter set (NTC) derived in the present work. 'Ref' denotes the reference lattice and the ρ_0 values specify the relative densities for each element in the alloy system. Note that the ternary set applies $\rho_0(Al) = 1.1$, but for the binary Al-Mg system this parameter was set to 1.0. The cut-off, r_c, was set to 4.0 Å for the ternary system, which is sufficient to include all unscreened interactions in $Mg_{1-x}Al_xB_2$. The α parameter is defined by $\alpha^2=9\Omega B/E_c$, where Ω is the atomic volume, B is the bulk modulus and E_c is the cohesive energy for the alloy system in the reference lattice. The r_e parameter is the equilibrium distance between unlike atoms in the alloy reference lattice.

	E_c	Ref	r_c	α	r_e	ρ_0
Al-Mg	-0.55	B1	5.0	4.17	3.378	1.0,0.6
Mg-B	0.33	B1	4.0	4.00	2.478	0.6,7.0
Al-B	0.22	B1	4.0	4.20	2.3015	1.1,7.0

Table 3: The thermodynamic consistent set Mg-Al-B parameter set (TC) derived in the present work. See Table 2 for parameter definitions.

	$C_{min}(1,2,1)$	$C_{min}(2,1,2)$	$C_{min}(1,1,2)$	$C_{min}(1.2,2)$	$C_{max}(1,2,1)$	$C_{max}(2,1,2)$	$C_{max}(1,1,2)$	$C_{max}(1,2,2)$
Mg-Al	0.00	2.00	2.00	2.00	2.80	2.80	2.80	2.80
Mg-B	1.20	2.00	2.00	2.00	2.80	2.80	2.80	2.80
Al-B	1.00	2.00	2.00	2.00	2.80	2.80	2.80	2.80

Table 4: The Mg-Al-B screening parameters for the non-thermodynamic consistent set (NTC). The C(i,j,k) parameters specify how the i-j atom pair is screened by atom k, see for example Ref. 39,43 for parameter definitions. The parameters that are not listed were set to the default values of C_{min}=2.0 and C_{max} = 2.8.

	$C_{min}(1,2,1)$	$C_{min}(2,1,2)$	$C_{min}(1,1,2)$	$C_{min}(1,2,2)$	$C_{max}(1,2,1)$	$C_{max}(2,1,2)$	$C_{max}(1,1,2)$	$C_{max}(1,2,2)$
Mg-Al	0.00	2.00	3.1	3.1	2.80	2.80	3.10	3.10
Mg-B	1.20	2.00	2.00	2.00	2.80	2.80	2.80	2.80
Al-B	1.00	2.00	2.00	2.00	2.80	2.80	2.80	2.80

Table 5: The Mg-Al-B screening parameters for the thermodynamic consistent set (TC), see Table 4 and for example Ref. 39,43 for parameter definitions. The "unusual" C_{min} and C_{max} values of 3.1 were chosen to induce complete in-plane screening. This approach is further discussed in the Results/Discussion section.

All density functional theory (DFT) calculations were performed with the Vienna ab-initio simulation package (VASP)[44,45,46] using the projector augmented wave (PAW) method.[47,48] The generalized gradient approximation (PBE-GGA)[49,50] was used to describe the exchange-correlation effects. For the binary MgB_2 and AlB_2 C32 structures we used a 19×19×19 Gamma-point centered k point mesh and for ordered $Mg_{0.5}Al_{0.5}B_2$ the $Mg_{0.5}Al_{0.5}B_2$(anti) compound (see Sec. Results/Discussion) we applied 13×13×7 and 7×13×7 Gamma-point centered meshes, respectively. The binary MgB and AlB B1 (NaCl) structures were described with a 19×19×19 Monkhorst Pack k point mesh. For all compounds the Brillouin-zone integration was performed using the Methfessel-Paxton smearing scheme with a smearing parameter of 0.20 eV[51] and the plane-wave cut-off energy was set to 318.606 eV, which is sufficient to reach convergence for all relative energies (formation energies), lattice parameters and elastic properties. Unless otherwise stated, the formation energies (E) are calculated with the pure elements in the fcc lattice as the reference state. For each structure, the equilibrium volume was determined by optimizing all internal structural parameters, i.e. both the shape of the unit cell and the atomic positions, at constant cell volume and then minimizing the energy by performing the same procedure at several cell volumes close to the equilibrium. The internal structural parameters were relaxed until the Hellmann-Feynman forces on each atom were negligible (<0.01 eV/Å). The bulk modulus was evaluated by a fit to the Murnaghan equation of state[52] and the elastic constants of the

cubic B1 structures (C' = $(C_{12}-C_{22})/2$ and C_{44}) were derived by fitting a quadratic polynomial to the calculated volume-conserving orthorhombic and tetragonal distortion curves.[53] The charge transfer analysis was performed within the Bader approach to charge decomposition.[54]

The $Mg_{1-x}Al_xB_2$ structures that contain nano-scale heterogeneities were modeled using 70×70×40 and 50×50×44 expansions of the primitive C32 unit cell, which correspond to 588000 and 330000 atoms in the simulation box, respectively. All diffraction spectra were calculated using the former model and the solution thermodynamics were studied within the latter model. The larger simulation box applies the NTC parameter set, while, since the TC set cannot treat as many atoms as the NTC set, we are forced to use the smaller model system for studying solution thermodynamics. Our intention is to simulate random distributions of the nano-scale inhomogeneities, however, the use of periodic boundary conditions inevitably introduces an "artificial" periodicity to our system. The size of our two simulation boxes are taken to be large enough to minimize unwanted effects arising from the periodic boundary conditions, while, at the same time, keeping the simulations computationally tractable. The powder diffraction spectra, i.e. no crystal orientation dependence is taken into account, for ordered compounds (MgB_2, AlB_2 and $Mg_{0.5}Al_{0.5}B_2$) are straight-forward to calculate as the averaged structure factor of all atom pairs in the unit cell, S(Q), where Q is the scattering vector.[30,55] Even though the scattering power of individual atoms are different, in the present work we have assumed this parameter to be unity for all atom types. This "brute force" calculation of total structure factors becomes extremely time-consuming for systems with large simulation boxes and must be circumvented. Moreover, the "artificial" periodicity due to periodic boundary conditions introduce superlattice reflections, and, even though these are of small amplitude compared to major diffraction peaks, they make interpretation of the fine structures, e.g. peak asymmetries and peak splits, difficult. These issues can be circumvented by instead calculating the total structure factor (i.e. the powder diffraction pattern) as the Sine transform of the pair distribution function, $\rho(r)$, for the relaxed structures.[30,55] In order to obtain adequate Q resolution for

S(Q), $\rho(r)$ must be calculated up to a sufficiently large radius, r_{max}. However, in order to avoid effects of the periodic boundary conditions, r_{max} must also fulfill $r_{max} < R_{min}/2$, where R_{min} is the shortest periodicity in the simulation box, which implies that r_{max} is limited by the size of our simulation box. Unfortunately, since the number of atoms that we can treat in our simulations is limited, in order to reach sufficient Q resolution, we have relaxed the requirements imposed on r_{max} by the periodic boundary conditions. In practice we allowed r_{max} to reach $4 \cdot R_{min}$. Test calculations showed that errors resulting from introducing slight periodicity in $\rho(r)$ are small and do not infer our conclusions. Still, even with the simplifications stated above, calculating $\rho(r)$ with $r_{max} = 4 \cdot R_{min}$ for about half a million atoms is not feasible due to the excessive computational time that is required, however we are able to avoid this problem by calculating $\rho(r)$ for a subset of atoms. In order to make sure that we obtain representative statistics we randomly sample 30000 atoms among the total of approximately half a million atoms. In order to remove small oscillations in the Fourier transform of $\rho(r)$ a smearing factor is applied, which gives rise to slight widening of the calculated diffraction peaks (see for example the calculated S(Q) for MgB_2 in Fig. 12). In order to facilitate impartial comparison of the S(Q) spectra, they were all calculated with the same set of parameters, which implies that any artificial widening or smearing of diffraction peaks should be similar for all samples, thus enabling us to detect features that are caused by structural differences at the nano-scale.

In order to investigate the $Mg_{1-x}Al_xB_2$ ground-state structures as function of composition and temperature we have performed Metropolis Monte Carlo simulations using the Mg-Al-B MEAM potentials. The simulations were carried out within the canonical ensemble. Consequently, the volume of the simulation cell was kept constant during each Monte Carlo (MC) run and the contraction in the c direction associated with the redistribution of Al and Mg atoms between different planes was instead accounted for by performing a sequence of MC simulations with static relaxations in-between each run. This approach mimics zero-pressure conditions. The Monte Carlo simulation procedure that we have

applied to $Mg_{1-x}Al_xB_2$ is derived from the approach described by Wang *et al.* in Ref. 56. In each Monte Carlo step we allow for exchange of randomly selected Al and Mg atomic species (only different atomic species are allowed to exchange position) and for spatial displacements of a randomly selected atom (the displacement direction was randomly distributed and the displacement distance was selected at random within the 0.00, 0.10 Å interval). The first process accounts for inter-diffusion of Al/Mg and the second process for structural relaxation and thermal vibrations. The average number of sampling steps per atom in our simulations was approximately 5000, after which only minor changes in the Al/Mg distribution and the total energy could be observed and thus we assumed that the equilibrium state had been reached. We performed simulations for x_{Al} = 0.05, 0.10, 0.25 and 0.50 within a simulation box containing 4320 atoms. Each simulation was performed at four temperatures, 298, 500, 750 and 900 K, which provides us with a coarse but qualitative understanding of the phase diagram. We also carried out the same type of Mont-Carlo simulations using a larger simulation box of 38400 atoms in order to verify any size dependence.

Results and discussion

DFT calculations for MgB_2, AlB_2 and $Mg_{0.5}Al_{0.5}B_2$

In order to obtain thermodynamic and structural data to be used for fitting of the Mg-Al-B MEAM potentials, we have applied DFT calculations to estimate the formation energy (E), the bulk modulus (B) and the lattice parameters (a and c) of MgB (B1 structure), AlB (B1 structure), MgB_2 (C32 structure) and AlB_2 (C32 structure), respectively. For MgB(B1) and AlB(B1) the elastic constants ($C'=(C_{11}-C_{12})/2$ and C_{44}) were also calculated. Additionally, the ordered $Mg_{0.5}Al_{0.5}B_2$ compound as well as the $Mg_{0.5}Al_{0.5}B_2$ anti-site energy, i.e. the energy associated with exchanging Al and Mg atoms between the ordered hexagonal Mg and Al planes [labeled $Mg_{0.5}Al_{0.5}B_2$(anti)], have been studied. In our model structure the concentration of anti-site defects was assumed to be ½ and the anti-sites constitute alternating linear chains within the hexagonal Mg/Al plains. These chains are shifted one step with respect to the chains in neighboring Mg/Al planes. The calculated properties for the Mg-Al-B system

are summarized in Table 6 together with available experimental data. For MgB_2, AlB_2 and $Mg_{0.5}Al_{0.5}B_2$ there is excellent agreement with experiments for the structural and elastic properties. Our calculations also reproduce earlier theoretical results for MgB_2[57,58] and AlB_2.[59] The $Mg_{0.5}Al_{0.5}B_2$(anti) compound is, as expected, less stable than $Mg_{0.5}Al_{0.5}B_2$. The MgB and AlB B1 structures are meta-stable with respect to phase separation into the pure elements, as indicated by the positive formation energies. In fact, the negative shear modulus (C_{44}) in Table 6 indicates that these compounds are even dynamically unstable.

In order to derive a MEAM B potential we have studied a number of B polymorphs (hcp, bcc, simple cubic, diamond, dimer, graphite, graphene, T-50 and fcc) in terms of their thermodynamic (formation energies), elastic (bulk moduli and elastic constants for the diamond structure) and structural properties (lattice parameters for all phases). In agreement with experiments we predict the so-called T-50 structure to be the most stable B polymorph (at least out of the phases studied in this work).[60] Further details of the B studies and the derivation of the B potential will be presented elsewhere.[61]

	a (Å)	c/a	E (eV)	B (GPa)	C_{44} (GPa)	C' (GPa)
MgB (B1)	4.896	—	0.10	68.3	-27.7	49.75
MgB_2 (C32)	3.077 (3.086)[1,62]	1.145 (1.142)[1,62]	-1.04	142.6 (151)[1,62]	—	—
AlB (B1)	4.543	—	-0.01	124.2	-20.9	106.6
AlB_2 (C32)	3.0008 (3.009)[63]	1.096 (1.084)[63]	-0.94	172.9 (170)[64]	—	—
$Mg_{0.5}Al_{0.5}B_2$	3.050 (3.04436)[3]	2.220 (2.204)[3]	-1.059 -0.070*	167.2	—	—
$Mg_{0.5}Al_{0.5}B_2$ (anti-site)	3.050	2.220	-1.032 -0.042*	163.4	—	—

Table 6: Properties of various Mg-Al-B compounds calculated from DFT. '—' indicates that this property was either not calculated or not defined for a particular compound. All energies apply the pure elements in the fcc lattice as the reference state. Where available, experimental values are given within parenthesis. The numbers labeled by * for $Mg_{0.5}Al_{0.5}B_2$ represent the solution energy with respect to

MgB_2 and AlB_2.

Fitting of the MEAM potential

Tables 1, 2, 3, 4 and 5 contain the fitted Mg-Al-B MEAM parameter sets and Tables 8 and 9 list the structural, elastic and thermodynamic properties that they predict, to be compared with the experimental/theoretical data in Tables 6 and 7. The Mg, Al and Mg-Al MEAM potentials were slightly adjusted from earlier works[43] in order to describe the thermodynamic properties of the borides more accurately. Even after these adjustments, the potentials give reasonable predictions for the Mg and Al subsystems, though, as discussed below, the changes applied to Mg-Al for the TC set introduce rather substantial deviations from the original potentials and thus render an inadequate description of the Mg-Al subsystem. The NTC set maintains the original potential for Mg-Al, but, as a consequence, it fails to capture the correct MgB_2-AlB_2 solution thermodynamics. The Mg-B and Al-B potentials were fitted to the DFT data for the B1 and C32 structures in Table 6. The agreement between the MEAM predictions and the calculated/experimental data is in most cases good, though for both MgB(B1) and AlB(B1) the empirical potentials fail to capture the negative C_{44} values predicted by the DFT calculations. The best compromise that could be attained was to adjust the MEAM potentials so that they predict C_{44} values close to zero and thus, at least partially, account for the soft nature of this deformation mode. There are also some minor discrepancies for the balance between the structural parameters for $Mg_{0.5}Al_{0.5}B_2$ and $Mg_{0.5}Al_{0.5}B_2$(anti), which, somewhat unexpected, are very similar according to the DFT calculations. In order to represent the stability of the $Mg_{0.5}Al_{0.5}B_2$ and $Mg_{0.5}Al_{0.5}B_2$(anti) compounds relative MgB_2 and AlB_2 appropriately, we were forced to choose a special form of the $C_{min}(1,1,2)$, $C_{min}(1,2,2)$, $C_{max}(1,1,2)$ and $C_{max}(1,2,2)$ MEAM screening parameters (see Table 5). This choice implies that the in-plane Mg-Al interactions are completely screened, while the Mg-Al interaction between atoms sitting on top of each other in nearest neighbor metal planes is not screened at all. The rationale for this choice is that in order to obtain negative solution energy for $Mg_{0.5}Al_{0.5}B_2$ relative MgB_2 and AlB_2, the Mg-Al interaction must be stabilizing (negative), however, unless the in-plane Mg-Al interactions are appropriately screened,

the anti-site defect structure, $Mg_{0.5}Al_{0.5}B_2$(anti), is always more stable than $Mg_{0.5}Al_{0.5}B_2$, which follows from the dominant nature of the in-plane compared to the inter-planar Mg-Al interactions. For the complete screening model optimal thermodynamic description of the ground-state $Mg_{0.5}Al_{0.5}B_2$ and $Mg_{0.5}Al_{0.5}B_2$(anti) properties requires slight adjustment of the α(Mg,Al), r_e(Mg,Al) and E_c(Mg,Al) parameters (see Table 3). This parameter set is labeled thermodynamic consistent set (TC) owing to its ability to predict the correct energy balance between $Mg_{1-x}Al_xB_2$, $Mg_{0.5}Al_{0.5}B_2$ and the pure end-member compounds. As mentioned above, we have also used a MEAM potential with conventional screening parameters, for which the α(Mg,Al), r_e(Mg,Al) and E_c(Mg,Al) parameters were taken directly from DFT calculations for the Mg-Al subsystem, i.e. the meta-stable MgAl(B1) structure. This set is labeled non-thermodynamic consistent set (NTC), since the $Mg_{1-x}Al_xB_2$ energy balances are not correctly described, however as emphasized in Table 9 the two potential sets predict very similar structural properties. From this we conclude that the NTC potential set can be used for studying structural properties of prescribed atomic distributions, e.g. relaxation of Al-doped MgB_2, while the TC potential set must be applied in order to capture the thermodynamic stability of MgB_2-AlB_2 solid solutions and the ordered $Mg_{0.5}Al_{0.5}B_2$ compounds. For both potential sets the Al-B bond distance, r_e(Al,B), is given a slightly higher value than that predicted from the DFT calculations (2.3015 Å vs. 2.2715 Å) and the reason for this choice is that a small structural instability occurred for the B atoms in AlB_2 when the exact value from the DFT calculations was used. By increasing r_e(Al,B) by 0.03 Å and adjusting ρ_0(Al,B) to 1.1 this instability could be avoided, without causing sizeable deviations of any other properties listed in Tables 8 and 9. In order to maintain the appropriate structural relation between MgB_2 and AlB_2, as obtained from both experiments and DFT, we slightly adjusted the r_e(Mg,B) parameter (from 2.448 Å to 2.478 Å), since the difference in the a and c/a lattice parameters between MgB_2 and AlB_2 would otherwise be incorrectly represented.

	a (Å)	c/a	E (eV)	B (GPa)	C_{44} (GPa)	C' (GPa)
MgB (B1)	4.956	—	0.10	60	10	23.8
MgB_2 (C32)	3.077	1.145	-3.11	139	—	—

AlB (B1)	4.600	—	-0.01	108	12	49.3
AlB_2 (C32)	3.001	1.096	-2.827	188	—	—
$Mg_{0.5}Al_{0.5}B_2$	3.115	2.23	-0.066	164.2	—	—
$Mg_{0.5}Al_{0.5}B_2$ (anti)	3.068	2.31	-0.038	161.24	—	—

Table 8: The properties of various Mg-Al-B compounds, as predicted from the thermodynamic consistent (TC) MEAM potentials. All formation energies use the pure elements in the fcc lattice as the reference state. The values in this table should be compared to the corresponding DFT values in Table 6.

	a (Å)	c/a	E (eV)	B (GPa)	C_{44} (GPa)	C' (GPa)
MgB (B1)	4.956	—	0.10	60	10	23.8
MgB_2 (C32)	3.077	1.145	-3.11	139	—	—
AlB (B1)	4.600	—	-0.01	108	12	49.3
AlB_2 (C32)	3.001	1.096	-2.827	188	—	—
$Mg_{0.5}Al_{0.5}B_2$	3.100	2.22	0.010	162.13	—	—
$Mg_{0.5}Al_{0.5}B_2$ (anti)	3.065	2.301	0.034	159.49	—	—

Table 9: The properties of various Mg-Al-B compounds, as predicted from the non-thermodynamic consistent (NTC) MEAM potentials. All formation energies use the pure elements in the fcc lattice as the reference state. The values in this table should be compared to the corresponding DFT values in Table 6.

Structure and stability of nano-scale heterogeneities in $Mg_{1-x}Al_xB_2$

The nano-scale heterogeneities that have been considered in this work include two different geometries; hexagons and stripes, and for each case we apply two different ordering patterns; pure Al domains and mixed domains where every other atom is either Mg or Al. In most of our simulations the hexagons/stripes are randomly distributed, with the additional condition that overlap is prohibited. In order to mimic the $Mg_{0.5}Al_{0.5}B_2$ ordering pattern we have also performed simulations in which the nano-scale Al domains are only allowed to occupy every second metal plane (compare with ordering into alternating pure Mg/Al planes in $Mg_{0.5}Al_{0.5}B_2$). Additionally, we have considered a couple of special

cases; $Mg_{1-x}Al_xB_2$ structures with Al atoms fully occupying a subset of planes and completely ordered $Mg_{0.5}Al_{0.5}B_2$ domains of 6-fold prismatic geometry embedded within the MgB_2 matrix. Below we focus the discussion on a few representative structure patterns within each class, however additional calculations were performed in order to underpin the conclusions drawn from these cases.

Fig. 10 plots the formation energy of a range of $Mg_{1-x}Al_xB_2$ compounds, as obtained from static relaxations (0 K), with respect to MgB_2 and AlB_2. The equilibrium state always involves MgB_2+$Mg_{0.5}Al_{0.5}B_2$ two-phase mixtures and for structures of intermediate Al concentration the excess energy relative MgB_2+$Mg_{0.5}Al_{0.5}B_2$ is closely correlated with the type of nano-scale Al structure pattern. Low excess energy is achieved for pure Al domains and the excess energy decreases with the size of these domains. Moreover, the excess energy is further decreased by allowing the pure Al domains to separate into every second Mg/Al plane, as for the ordered $Mg_{0.5}Al_{0.5}B_2$ compound. The lowest energy is obtained for structures with planes that contain only Al atoms, thus being a partial phase transformation into MgB_2+$Mg_{0.5}Al_{0.5}B_2$. Our calculations also show that hexagons are always more stable than stripe patterns, which is a consequence of the smaller area of each coherent Al domain for stripes than for the hexagons. Large Al domains facilitate efficient relaxation of the Al-B bond distance and thus enable these domains to imitate the Al-B interactions in $Mg_{0.5}Al_{0.5}B_2$, which explains the high stability of structure patterns that fulfill this condition. At the opposite end, random solid solutions impede relaxation of Al-B bond distances, yielding high excess energies. Mixed Mg/Al domains exhibit excess energies that are very close to the corresponding random solid solutions. The correlation between excess energies and relaxation of Al-B bond distances imply that the excess energy can equivalently be visualized in terms of the local strain. Fig. 11 plots the local strain, defined for each atom as the deviation of the average nearest neighbor Mg/Al-B distance from the nearest neighbor Mg/Al-B distance in MgB_2/AlB_2. Comparing with Fig. 10, we conclude that there is significant strain for structures with high excess energy, and, correspondingly, there is minimal strain for structures with low

excess energy.

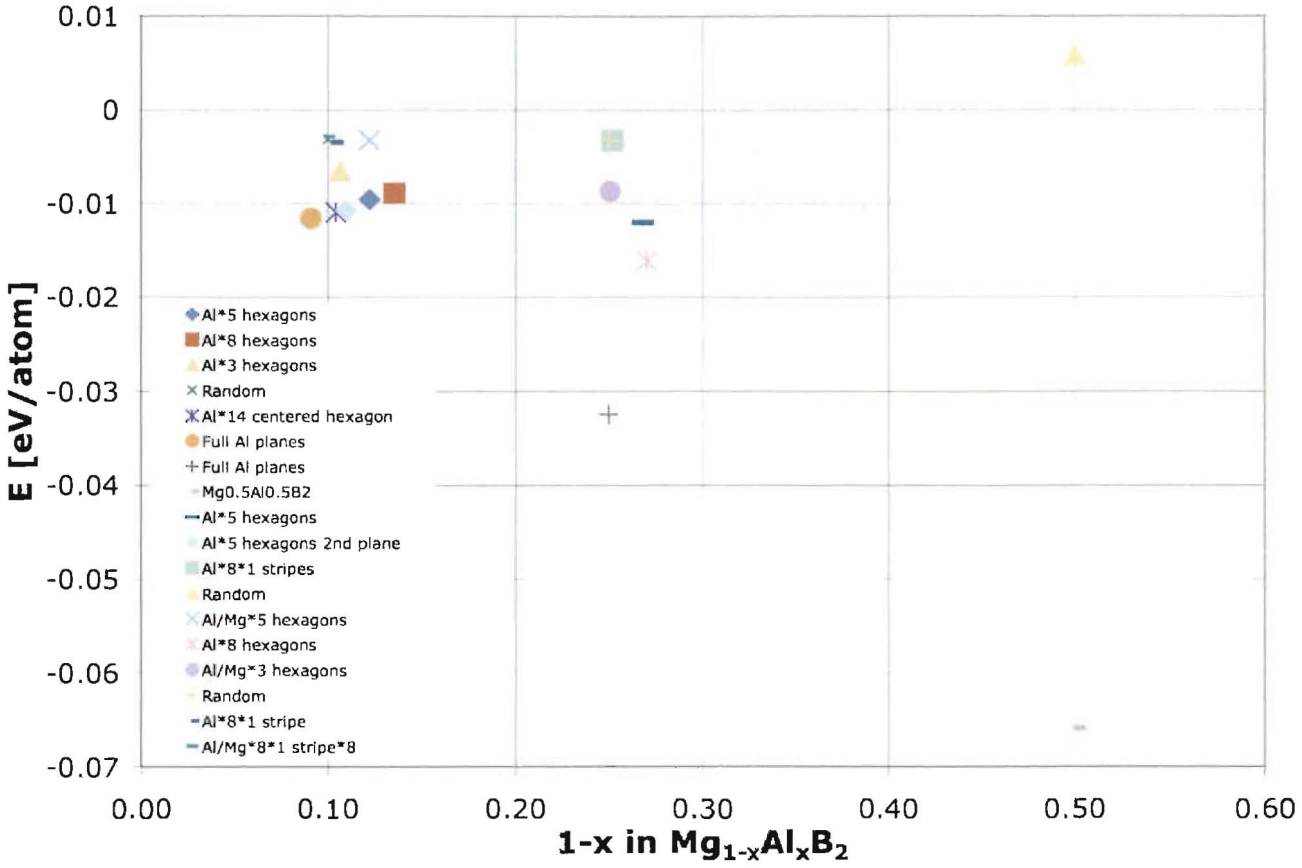

Fig. 10: The formation energy of a few representative $Mg_{1-x}Al_xB_2$ structure patterns with respect to MgB_2 and AlB_2. The number following the '*' in the legend denotes the size of the Al or Al/Mg domain. The zero-line indicates the position of an ideal MgB_2-AlB_2 solid solution.

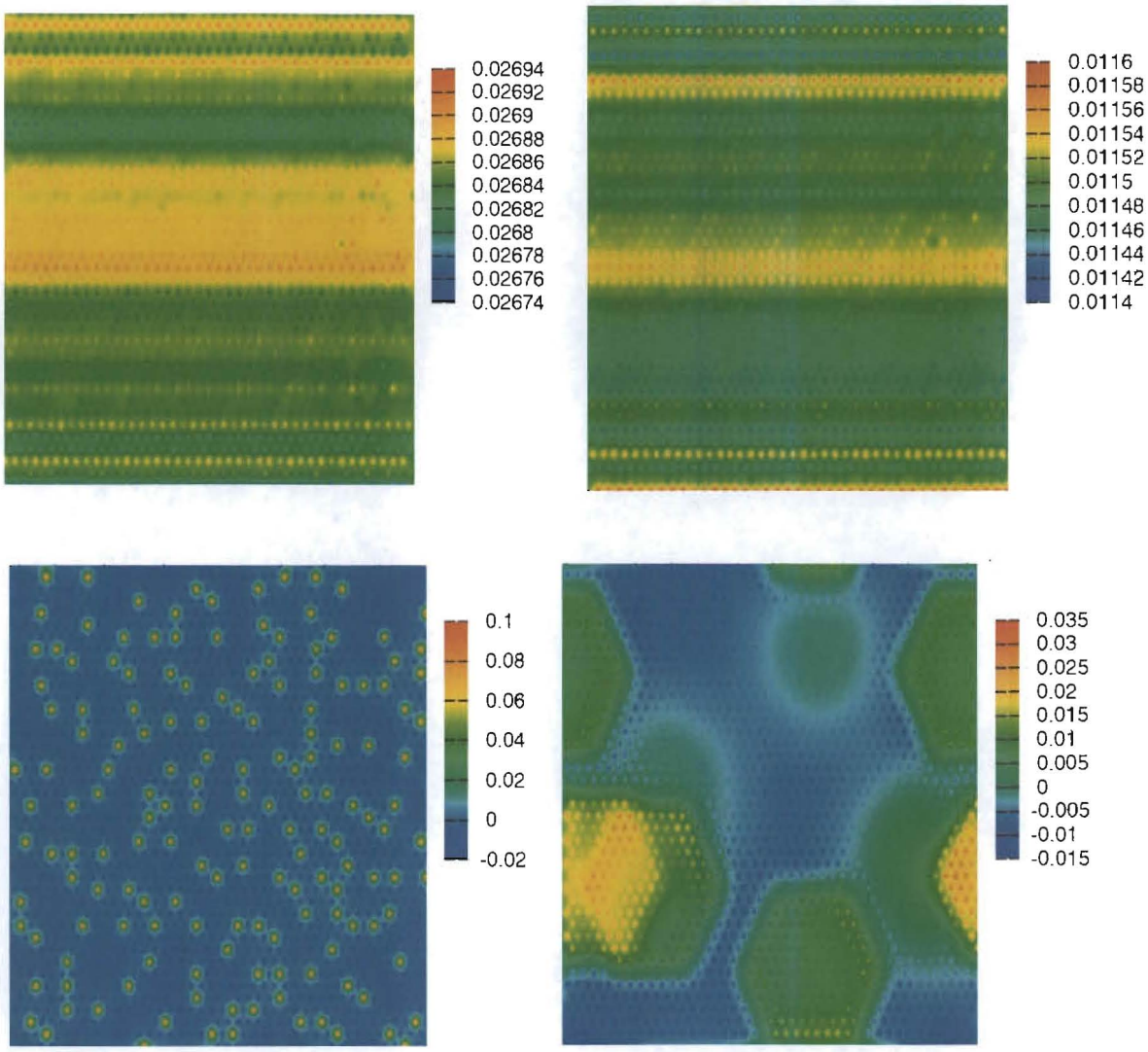

Fig. 11: Strain maps of various $Mg_{1-x}Al_xB_2$ compounds (see text for definition). Each plot represents the strain in a particular metal plain, i.e. a cut along the a-b plane of the hexagonal AlB_2 lattice. The c direction is perpendicular to the plane of the paper. a) Al planes in $Mg_{0.5}Al_{0.5}B_2$ b) Mg planes in $Mg_{0.5}Al_{0.5}B_2$ c) A Mg/Al plane in $Mg_{0.90}Al_{0.10}B_2$ with randomly distributed Al atoms, d) A Mg/Al plane in $Mg_{0.90}Al_{0.10}B_2$ with Al hexagons of size 8 in every second Mg plane. The strain is small for $Mg_{0.50}Al_{0.50}B_2$ compounds, which follows from the ability to individually relax each plane containing either Mg or Al. Note that the strain is defined with respect bond distances in MgB_2 and AlB_2 and the positive strain values reflect that the optimal bond distances for $Mg_{0.50}Al_{0.50}B_2$ are slightly different than for the pure MgB_2 and AlB_2 compounds. The highest strain is observed for the random solid solution in c), which is due to the inability to relax the bond distances for individual Al atoms. Since the large Al

domains in d) are able to relax much more efficiently than the individual Al atoms in c), the strain is significantly smaller in d) than in c). In d) the hexagonal strain domains correspond to Al domains in the lattice and the varying magnitude of the strain originates from the distance of the Al hexagons to the particular B plane for which the strain is plotted. This highlights that the strain is not exclusively caused by the composition of the nearest neighbor planes, but second nearest neighbors also have a considerable impact.

Table 10 summarizes the results from the Monte Carlo simulations. At low temperature (T=298 K) our simulations predict phase separation into MgB_2+$Mg_{0.5}Al_{0.5}B_2$ for all Al concentrations that have been investigated (x_{Al}=0.05, 0.10, 0.25 and 0.50), though for x_{Al}=0.05 phase separation is only partial and there is a mixture of small $Mg_{0.5}Al_{0.5}B_2$ domains and randomly distributed Al atoms. The degree of disorder increases with increasing temperature and for low Al concentrations (x_{Al}=0.05) complete disorder develops from T=500 K. For higher x_{Al} we observe a two-phase $Mg_{1-x}Al_xB_2$+$Mg_{0.5}Al_{0.5}B_2$ state, where x (the concentration of Al in the random solid solution) increases with increasing temperature. From this we conclude that our simulations are in qualitative agreement with the experimental phase diagram, which exhibits a single phase field for $x_{Al}<0.10$, a two-phase field for $0.10<x_{Al}<0.25$ and an ordered $Mg_{0.5+y}Al_{0.5-y}B_2$ compound for $x_{Al}>0.25$.[3,18] However, we note that the simulated phase state for $x_{Al}< 0.10$ involves significant short range order and complete disorder is never attained at ambient conditions (T = 298 K). Our theoretical predictions seem to slightly overestimate tendencies towards ordering. In most of our simulations the equilibrium state in fact involves multiple $Mg_{0.5}Al_{0.5}B_2$ domains instead of one large domain, as would be expected for "complete" phase separation. The reason for the absence of $Mg_{0.5}Al_{0.5}B_2$ domain coalescence in our simulations is that when domains occupy different Al/Mg planes, i.e. when the respective $Mg_{0.5}Al_{0.5}B_2$ domains are out of phase with respect to the c lattice planes that they occupy, the current Monte Carlo simulations fail to capture domain growth/coalescence. Presently, we are unable to ascertain if this effect corresponds to a real physical phenomena or if it is an artifact of our simulations. In Table 10 we choose to interpret multiple large $Mg_{0.5}Al_{0.5}B_2$ domains that

coexist with $Mg_{1-x}Al_xB_2$ as complete phase separation. If the Monte Carlo simulations are started from an ordered MgB_2+$Mg_{0.5}Al_{0.5}B_2$ state instead of from a structure with randomly distributed Al atoms, the equilibrium state is essentially identical to the starting MgB_2+$Mg_{0.5}Al_{0.5}B_2$ state for both x_{Al}=0.25 and x_{Al}=0.50, which underlines our current interpretation of multiple large $Mg_{0.5}Al_{0.5}B_2$ domains as representing complete phase separation. However, the present results could also indicate that, even though there is a driving force to phase separate into $Mg_{1-x}Al_xB_2$+$Mg_{0.5}Al_{0.5}B_2$, the actual transformation may be inhibited due to slow domain growth and give rise to complex nano-scale structure patterns as well as significant short range order, in particular for small x_{Al}. This would be in line with the interpretation of experimental X-ray diffraction data offered by Margadonna *et al.*[3] and may also be connected to the modulation in the a-b planes discussed by Cava *et al.*[18,66]

X/T	298	500	750	900
0.05	Partial order ($Mg_{1-x}Al_xB_2$+$Mg_{0.5}Al_{0.5}B_2$, x<0.05); small domains of $Mg_{0.5}Al_{0.5}B_2$ and randomly distributed Al atoms within the MgB_2 matrix.	Disordered $Mg_{1-x}Al_xB_2$, no $Mg_{0.5}Al_{0.5}B_2$ domains.	Disordered $Mg_{1-x}Al_xB_2$, no $Mg_{0.5}Al_{0.5}B_2$ domains.	Disordered $Mg_{1-x}Al_xB_2$, no $Mg_{0.5}Al_{0.5}B_2$ domains.
0.10	Ordered $Mg_{0.5}Al_{0.5}B_2$ domains within the MgB_2 matrix.	Ordered $Mg_{0.5}Al_{0.5}B_2$ domains co-existing with randomly distributed Al atoms within the MgB_2 matrix ($Mg_{1-x}Al_xB_2$+$Mg_{0.5}Al_{0.5}B_2$).	Disordered $Mg_{1-x}Al_xB_2$, no $Mg_{0.5}Al_{0.5}B_2$ domains.	Disordered $Mg_{1-x}Al_xB_2$, no $Mg_{0.5}Al_{0.5}B_2$ domains.
0.25	Ordered $Mg_{0.5}Al_{0.5}B_2$ domains within the MgB_2 matrix.	Ordered $Mg_{0.5}Al_{0.5}B_2$ domains co-existing with randomly distributed Al atoms within the MgB_2 matrix ($Mg_{1-x}Al_xB_2$+$Mg_{0.5}Al_{0.5}B_2$).	Ordered $Mg_{0.5}Al_{0.5}B_2$ domains co-existing with randomly distributed Al atoms within the MgB_2 matrix ($Mg_{1-x}Al_xB_2$+$Mg_{0.5}Al_{0.5}B_2$). The fraction of random Al atoms is higher than for T=500 K.	Ordered $Mg_{0.5}Al_{0.5}B_2$ domains co-existing with randomly distributed Al atoms within the MgB_2 matrix ($Mg_{1-x}Al_xB_2$+$Mg_{0.5}Al_{0.5}B_2$). Complete disordering has occurred at 1000 K.
0.50	Ordered $Mg_{0.5}Al_{0.5}B_2$ domains within the MgB_2 matrix.	Ordered $Mg_{0.5}Al_{0.5}B_2$ domains within the MgB_2 matrix.	Ordered $Mg_{0.5}Al_{0.5}B_2$ domains within the MgB_2 matrix.	Ordered $Mg_{0.5}Al_{0.5}B_2$ domains within the MgB_2 matrix.

Table 10: Results from the Monte Carlo simulations.

Simulated diffraction patterns of nano-scale heterogeneities in $Mg_{1-x}Al_xB_2$

Figs. 12-16 plot the calculated structure factors, S(Q), within the 5.5 $Å^{-1}$< Q < 9.5 $Å^{-1}$ range for a number of representative $Mg_{1-x}Al_xB_2$ structures containing nano-scale heterogeneities and for comparison each figure also includes S(Q) for MgB_2, $Mg_{0.5}Al_{0.5}B_2$ and the corresponding $Mg_{1-x}Al_xB_2$

random solid solution. The S(Q) features emerging from the nano-scale structure patterns are in general somewhat more pronounced in the 5.5 $Å^{-1}$< Q < 9.5 $Å^{-1}$ range than for Q < 5.5 $Å^{-1}$. From Fig. 13 we conclude that mixed Mg/Al stripe and hexagon domains exhibit S(Q) spectra that are virtually identical to the corresponding random solid solutions, which correlates with the similarities between excess energies and lattice strains for these domains (see Fig. 10 and Fig. 11). The shifts of certain S(Q) peak positions for mixed Mg/Al domains and random solid solutions in relation to MgB_2 mainly follow from relaxation of the c lattice parameter (c/a ratio) as the fraction of Al increases. As previously mentioned, this is a consequence of the shorter Al-B compared to Mg-B bond distance. With the current Q resolution, we are unable to identify any evident peak asymmetries for structure patterns with mixed Mg/Al domains or for the random solid solutions. Structures composed of pure Al domains exhibit more significant shifts of the S(Q) spectra relative the random solid solutions and there are also symmetry/shape changes close to the base line for a number of the S(Q) peaks. These observations are illustrated in Fig. 12. The magnitude of the S(Q) shifts grows for increasing size of the pure Al domains, even though, according to Fig. 12, this effect is rather small. Comparing Figs. 12 and 16, we conclude that the peak shifts are always more significant for hexagons than for stripes, which is ascribed to the larger size of coherent Al domains for hexagons than for stripes. These observations correlate directly with the ability to efficiently relax the geometry of pure Al domains, as discussed above for the excess energies. By comparing the $Mg_{1-x}Al_xB_2$ S(Q) spectra for pure Al domains to the spectra for MgB_2, $Mg_{0.5}Al_{0.5}B_2$ and the random solid solutions, we conclude that the shifts for $Mg_{1-x}Al_xB_2$ with pure Al domains are such that the S(Q) peaks are positioned in-between the MgB_2 and $Mg_{0.5}Al_{0.5}B_2$ reference structures, and in relation to the corresponding peak positions for random solid solutions, the $Mg_{0.5}Al_{0.5}B_2$ character is much more evident. In addition to S(Q) peak shifts, the structures with large coherent domains of Al atoms exhibit splits of some diffraction peaks, e.g. around q=7 $Å^{-1}$ for $Mg_{0.75}Al_{0.25}B_2$ (x_{Al}=0.25) with pure Al hexagons of size 5 and 10, as illustrated in Fig. 12. These split features are also present for completely ordered $Mg_{0.5}Al_{0.5}B_2$ compounds, thus emphasizing the

$Mg_{0.5}Al_{0.5}B_2$ character of structure patterns consisting of large pure Al domains. The S(Q) peak splits in Fig. 12 refer to structures with x_{Al}=0.25, in contrast Fig. 13 illustrates that for x_{Al}=0.10 there are no corresponding split S(Q) peaks for any of the nano-scale structure patterns, not even for large coherent Al domains. This emphasizes that the S(Q) features are not only a function of domain size and character, but also a function of the total Al concentration in $Mg_{1-x}Al_xB_2$, and most probably the splitting of certain peaks is triggered by the degree of c axis relaxation. There are small distortions of some S(Q) peaks even for x_{Al}=0.10, e.g. for q=7 $Å^{-1}$, which should be related to emerging peak splits and thus a signature of the $Mg_{0.5}Al_{0.5}B_2$ character, but these features are less pronounced than for higher x_{Al}. Despite being able to identify some S(Q) peak splits when the Al domains reach sufficiently large sizes and x_{Al} exceeds some threshold value, the unique superlattice peaks found in ordered $Mg_{0.5}Al_{0.5}B_2$, for example around q=7.5 $Å^{-1}$, are not visible for any of the structure patterns in Figs. 12 or 13. In some cases very small "ripples" that mark the existence/position of the unique $Mg_{0.5}Al_{0.5}B_2$ S(Q) features can be identified, but there are no unambiguous superlattice peaks. For structures with large Al domains situated in every second metal plane there are more significant indications of the superlattice peaks observed for $Mg_{0.5}Al_{0.5}B_2$ (see Fig. 14). In order to further investigate under what conditions the unique $Mg_{0.5}Al_{0.5}B_2$ features appear we constructed two test cases for x_{Al} = 0.25; one containing large Al hexagons that are situated on top of each other in every second plane, forming a large $Mg_{0.5}Al_{0.5}B_2$ domain shaped as a 6-sided prism, and another case where the Al atoms fully occupy every second plane in one half of the supercell. The first structure corresponds to a domain of $Mg_{0.5}Al_{0.5}B_2$ embedded within the MgB_2 matrix and the latter structure is identical to a separated $Mg_{0.5}Al_{0.5}B_2$ phase domain, effectively occupying half of the simulation box and the other half representing MgB_2. The structure containing full Al planes represents a semi-infinite $Mg_{0.5}Al_{0.5}B_2$ phase domain, while the extension of the $Mg_{0.5}Al_{0.5}B_2$ domain shaped as a 6-sided prism is bounded in every direction by the MgB_2 matrix. Fig. 15 demonstrates that both of these model structures give rise to peak splits that can be associated with ordered $Mg_{0.5}Al_{0.5}B_2$ (see discussion above), however only the structure with full Al planes give

rise to the unique smaller amplitude superlattice reflections observed for $Mg_{0.5}Al_{0.5}B_2$. Additionally, Fig. 15 highlights that only the structure containing full Al planes shows signatures of two phases, corresponding to MgB_2 and $Mg_{0.5}Al_{0.5}B_2$, in the S(Q) spectra (see for example the S(Q) peaks just below q=6 $Å^{-1}$). This difference between bounded and semi-infinite $Mg_{0.5}Al_{0.5}B_2$ domains occurs in spite of the fact that the Al domains are of similar size for both structure patterns and, moreover, the total concentration of Al is identical. The explanation for this behavior is that pure Al planes allow optimal c/a relaxation and the corresponding S(Q) pattern thus develops $Mg_{0.5}Al_{0.5}B_2$+MgB_2 character, while the embedded domains are hindered to achieve the same type of relaxation by the surrounding MgB_2 matrix and thus the MgB_2+$Mg_{0.5}Al_{0.5}B_2$ character is not clearly revealed in the S(Q) spectra. From this we conclude that the $Mg_{0.5}Al_{0.5}B_2$ domains must be large enough (semi-infinite) or incorporate dislocation type defects, in order to be clearly detected by X-ray diffraction techniques, since only when these conditions are fulfilled can the lattice optimally relax the c/a ratio and develop two-phase MgB_2+$Mg_{0.5}Al_{0.5}B_2$ character. Analogous to these conclusions, Howell *et al.* concluded that the L_{10} S(Q) character of L_{10} domains embedded within a matrix fcc phase only emerged when dislocations were introduced at the phase boundaries to allow strain release and relaxation of the L_{10} domains.[30] Additionally, this reference showed that unless the domain size exceeded a threshold of approximately 280 Å the unique L_{10} features disappeared in the diffuse background, even when dislocations are present. With exception for the semi-infinite $Mg_{0.5}Al_{0.5}B_2$ domains, the domains studied in this work are significantly smaller than the limit stated above and it is consequently not surprising that the unique $Mg_{0.5}Al_{0.5}B_2$ superlattice reflections are absent.

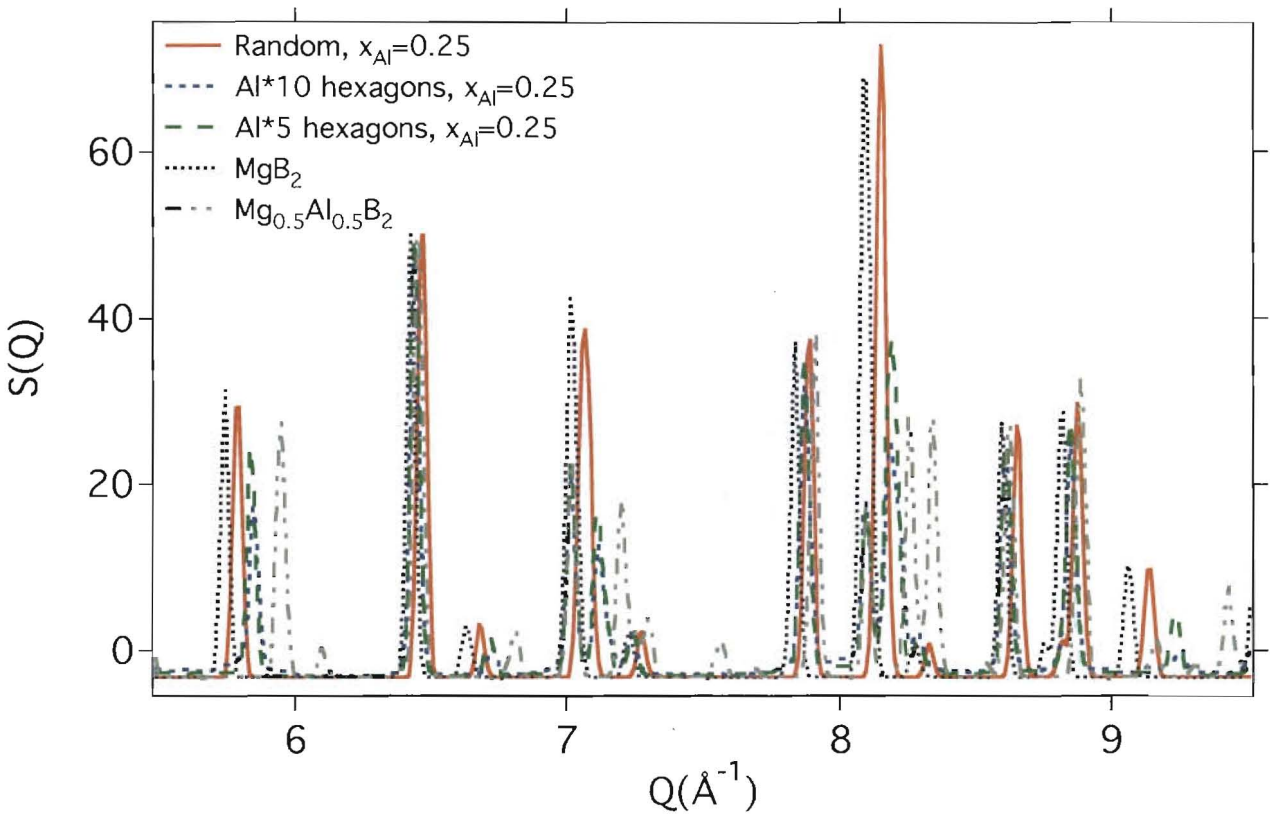

Figure 12: Simulated $Mg_{0.75}Al_{0.25}B_2$ (x_{Al}=0.25) S(Q) spectra for Al hexagons of size 5 and size 10, for comparison the S(Q) spectra for the x_{Al}=0.25 random solid solution, MgB_2, and $Mg_{0.5}Al_{0.5}B_2$ are also shown. Both Al hexagon structures deviate from the random solid solution and show certain features related to the ordered $Mg_{0.5}Al_{0.5}B_2$ compound, e.g. the three-peak structure around Q=7 Å^{-1}, while other $Mg_{0.5}Al_{0.5}B_2$ distinguishing features are missing, e.g. the superlattice peak at Q=7.5 Å^{-1}. Moreover, the $Mg_{0.5}Al_{0.5}B_2$ character slightly increases with the size of the Al hexagons.

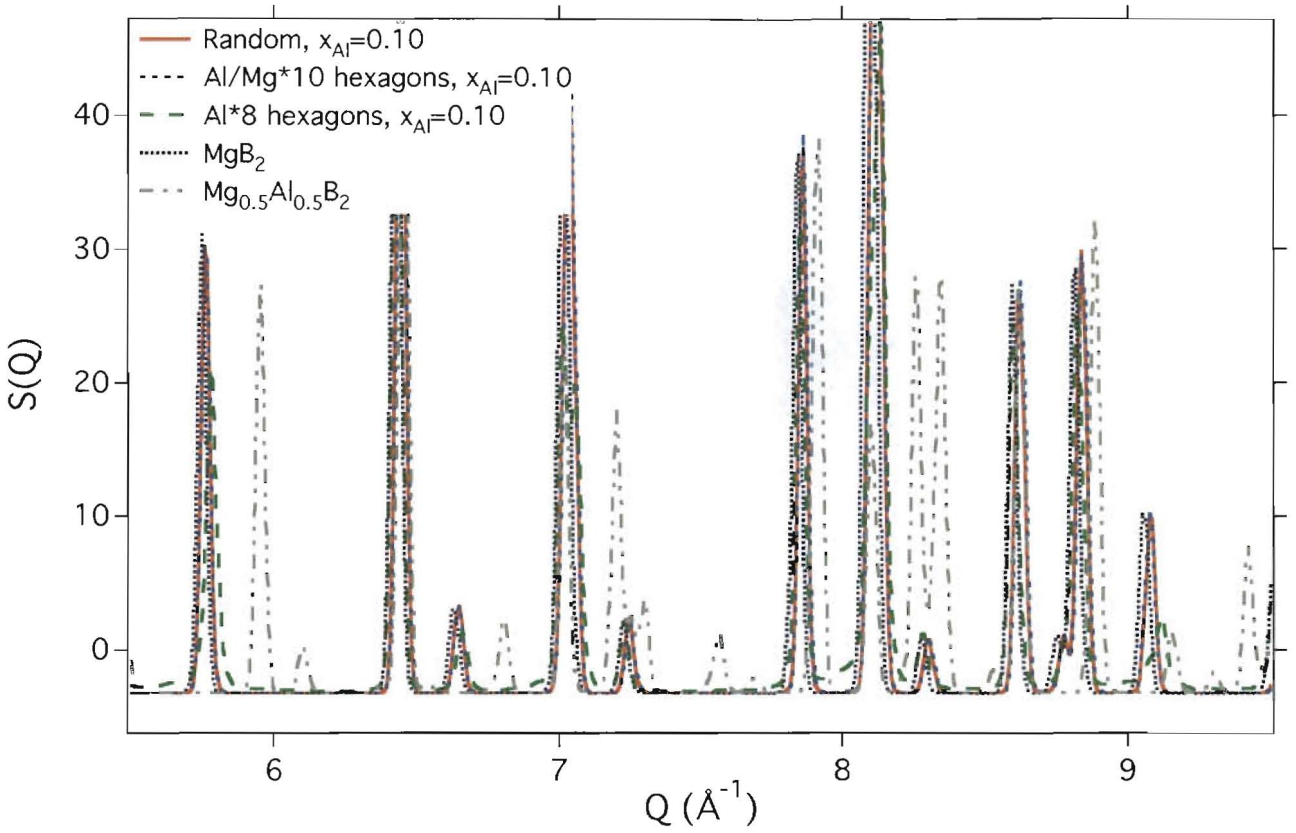

Figure 13: Simulated $Mg_{0.90}Al_{0.10}B_2$ (x_{Al}=0.10) S(Q) spectra for Al hexagons of size 8 and mixed Al/Mg hexagons of size 10, for comparison the S(Q) spectra for the x_{Al}=0.10 random solid solution, MgB_2, and $Mg_{0.5}Al_{0.5}B_2$ are also shown. The mixed hexagons overlay almost perfectly with the random solid solution, while the S(Q) spectra for Al hexagons exhibit somewhat larger shifts and distortions.

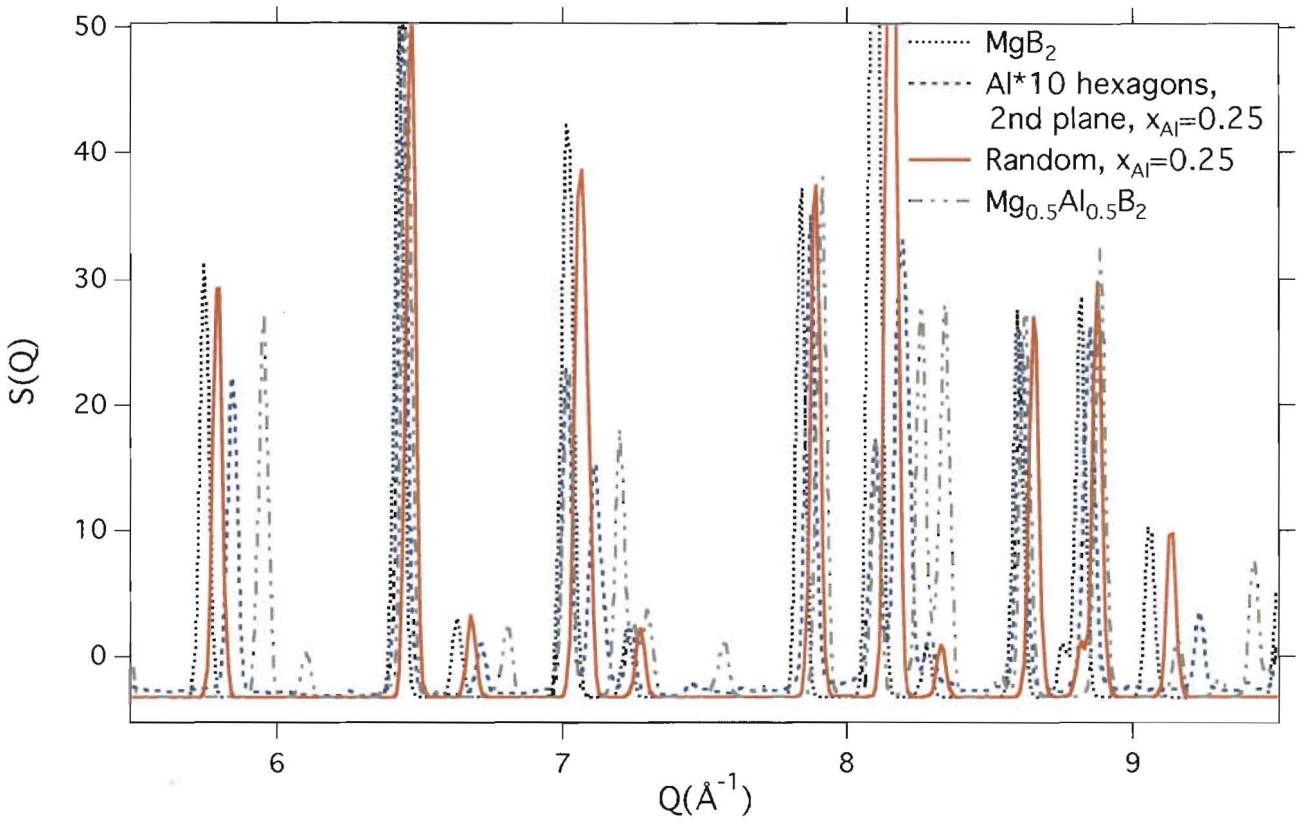

Figure 14: Simulated $Mg_{0.75}Al_{0.25}B_2$ (x_{Al}=0.25) S(Q) spectra for Al hexagons of size 10 that are only allowed to occupy every second metal plane of the $Mg_{0.75}Al_{0.25}B_2$ structure, for comparison the S(Q) spectra for the x_{Al}=0.25 random solid solution, MgB_2, and $Mg_{0.5}Al_{0.5}B_2$ are also shown.

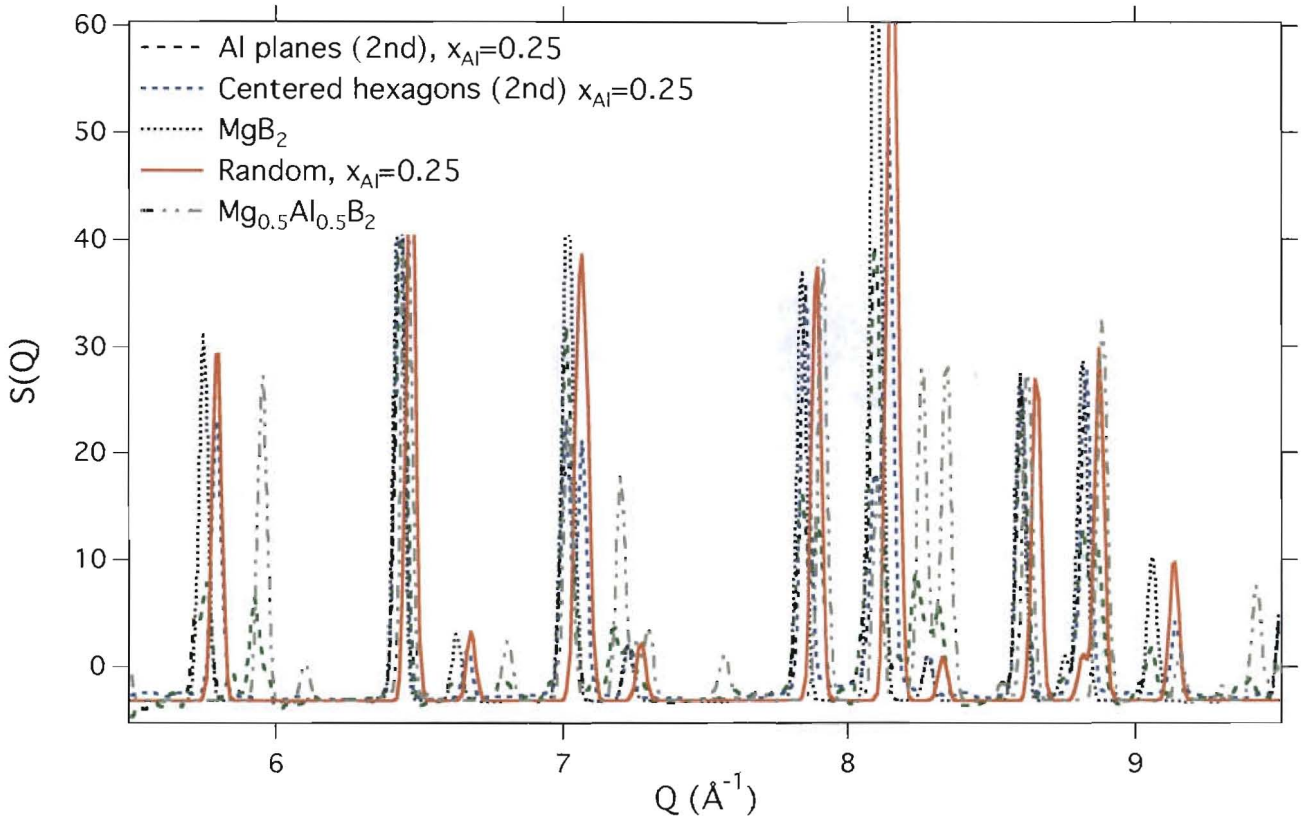

Figure 15: Simulated $Mg_{0.75}Al_{0.25}B_2$ (x_{Al}=0.25) S(Q) spectra for a structure where, for half of the supercell, every second metal plane is completely filled with Al atoms and every other plane only contains Mg atoms, thus representing a separated $Mg_{0.5}Al_{0.5}B_2$ phase domain and leaving the rest of the structure as pure MgB_2. The second $Mg_{0.75}Al_{0.25}B_2$ (x_{Al}=0.25) S(Q) spectra in this figure represents a structure with one large $Mg_{0.5}Al_{0.5}B_2$ domain embedded within the MgB_2 matrix in the form of a large 6-sided prism. For comparison the S(Q) spectra for the x_{Al}=0.25 random solid solution, MgB_2, and $Mg_{0.5}Al_{0.5}B_2$ are also shown. The structure with a semi-infinite $Mg_{0.5}Al_{0.5}B_2$ domain (Al planes (2^{nd})) exhibits both MgB_2 and $Mg_{0.5}Al_{0.5}B_2$ S(Q) features, while the fully embedded hexagonal $Mg_{0.25}Al_{0.25}B_2$ domain (centered hexagons (2^{nd})) correlates much closer with the x_{Al}=0.25 random solid solution.

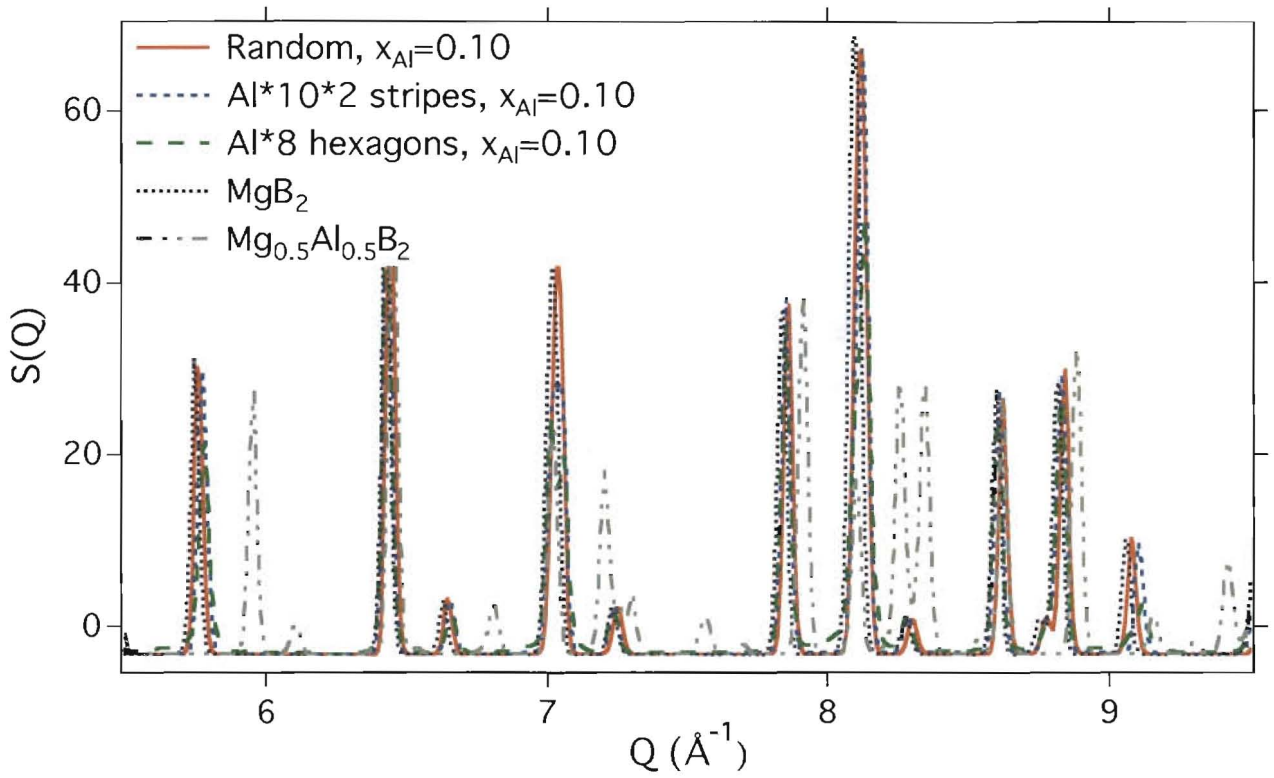

Figure 16: Simulated $Mg_{0.90}Al_{0.10}B_2$ (x_{Al}=0.10) S(Q) spectra for Al atoms clustered in the form of stripes, each with a length of 10 atoms and width of 2 atoms. The inclusion of the S(Q) spectra for Al hexagons of size 8 at x_{Al}=0.10 reveals that the S(Q) shifts/distortions are somewhat smaller for the stripe structure pattern than for hexagon based structures. This is an immediate consequence of the ability of hexagons to relax the c-lattice parameter more efficiently, owing the larger coherent domain size of the hexagons. For comparison the S(Q) spectra for the x_{Al}=0.10 random solid solution, MgB_2, and $Mg_{0.5}Al_{0.5}B_2$ are also shown.

Density of states and charge distribution for $Mg_{1-x}Al_xB_2$

In Ref. 32 Garcia-Adeva *et al.* demonstrated how the local electronic structure directly correlates with the local structure/ordering pattern for nano-scale L_{10} NiMn domains within the fcc NiMn random alloy. In order to explore how Al domains embedded inside a matrix of MgB_2 influence the electronic structure and local charge distribution, in particular the changes induced within the B planes, we have studied three $Mg_{1-x}Al_xB_2$ model compounds using the same type of density functional theory calculations as described above for MgB_2, AlB_2, $Mg_{0.5}Al_{0.5}B_2$, etc. All model compounds apply the 12×1×2 supercell

expansion of the primitive MgB_2 unit cell. The first model compound, labeled $Mg_{0.75}Al_{0.25}B_2$(A), contains a separate domain of AlB_2 that extends infinitely in two-dimensions (along the y- and z-axis), while it is bounded by the surrounding MgB_2 matrix in the third dimension (along the x-axis). The AlB_2 domain comprises three unit cells along the x-axis of the supercell and x_{Al}=0.25. The second model compound is labeled $Mg_{0.75}Al_{0.25}B_2$(B) and it is composed of a $Mg_{0.5}Al_{0.5}B_2$ domain that extends infinitely in two dimensions (along the y- and z-axis) while it is bounded in the third dimension (along the x-axis) by the MgB_2 matrix. For $Mg_{0.75}Al_{0.25}B_2$(B) the $Mg_{0.5}Al_{0.5}B_2$ domain comprises six unit cells along the x-axis of the supercell and x_{Al}=0.25. The third compound, $Mg_{0.875}Al_{0.125}B_2$(C), is analogous to $Mg_{0.75}Al_{0.25}B_2$(B) but with a $Mg_{0.5}Al_{0.5}B_2$ domain that is only half as wide and thus x_{Al}=0.125. As reference for our discussion, Fig. 17 illustrates the electronic density of states for MgB_2, AlB_2, ordered $Mg_{0.5}Al_{0.5}B_2$ and $Mg_{0.5}Al_{0.5}B_2$(anti). The electronic density of states at the Fermi level is lower for the AlB_2 and $Mg_{0.5}Al_{0.5}B_2$ compounds than for MgB_2, which primarily is a consequence of the increased electron transfer from Al to B ions, resulting in a downward shift of B orbitals relative the Fermi level, compared to MgB_2. The corresponding Bader charge density analysis, summarized in Table 7, confirms that the Al ions donate more electrons to the B planes than the Mg ions, however, since Al atoms also have one more valence electron than Mg atoms, the Al ions still retain more electrons than the Mg ions. Figs. 18, 19 and 20 plot the B partial density of states (PDOS) for $Mg_{0.75}Al_{0.25}B_2$(A), $Mg_{0.75}Al_{0.25}B_2$(B) and $Mg_{0.875}Al_{0.125}B_2$(C). The PDOS refer to four different B atoms that are located in the middle of the MgB_2 matrix (B1), at the MgB_2 side of the $MgB_2/AlB_2(/Mg_{0.5}Al_{0.5}B_2)$ interface (B2), at the $AlB_2(/Mg_{0.5}Al_{0.5}B_2)$ side of the $MgB_2/AlB_2(/Mg_{0.5}Al_{0.5}B_2)$ interface (B3) and finally in the middle of the $AlB_2(/Mg_{0.5}Al_{0.5}B_2)$ domain (B4), as illustrated in the inset of each figure (note that B3 and B4 are equivalent for $Mg_{0.75}Al_{0.25}B_2$(A)). Comparing with the DOS and PDOS for the bulk phases in Fig. 17 and by analyzing the corresponding Bader charge distribution in Table 12 the following trends emerge:

1) The $AlB_2/Mg_{0.5}Al_{0.5}B_2$ character increases from B1 to B4, which is seen as a shift of the PDOS in Figs. 18, 19 and 20 towards lower energy and larger B charge transfer in the Bader analyses. In

particular we notice the change in electronic properties as we cross the MgB_2-$Mg_{0.5}Al_{0.5}B_2$/AlB_2 interface, i.e. between B2 and B3.

2) The local AlB_2/$Mg_{0.5}Al_{0.5}B_2$ character increases with the size of the heterogeneous domain, which is seen as larger peak shifts and charge transfers for $Mg_{1-x}Al_xB_2$(B) than for $Mg_{1-x}Al_xB_2$(C).

3) The characteristics of the embedded AlB_2/$Mg_{0.5}Al_{0.5}B_2$ domains never reach the corresponding bulk AlB_2/$Mg_{0.5}Al_{0.5}B_2$ properties.

These conclusions emphasize that the strain distribution and thermodynamic stability of nano-scale structure domains are also reflected in the local electronic structure and charge distribution, which should give rise to strictly local character of various derived properties, such as electrical conductivity.

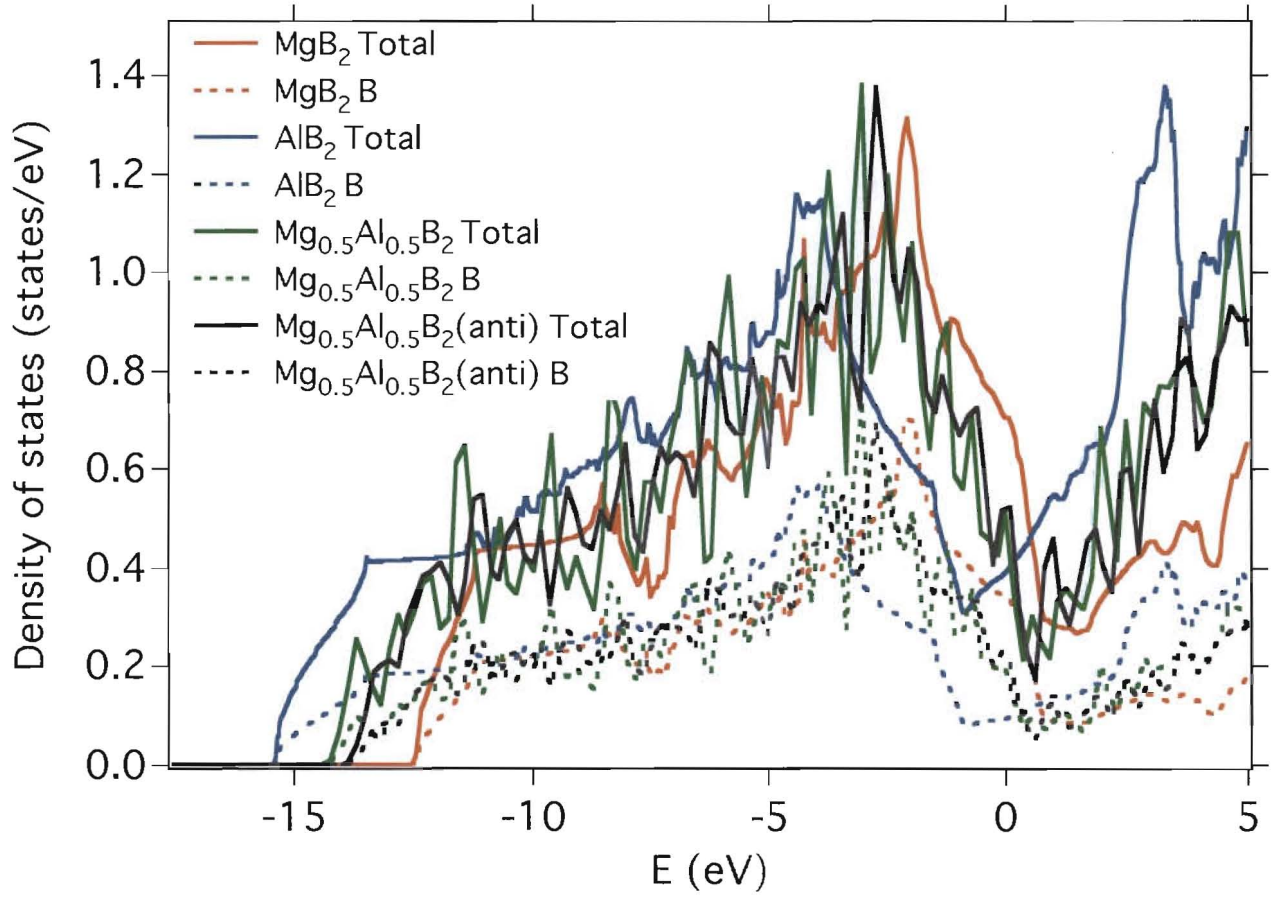

Figure 17: The density of states (DOS) and projected B density of states (PDOS) for MgB_2, AlB_2, $Mg_{0.5}Al_{0.5}B_2$ and $Mg_{0.5}Al_{0.5}B_2$(anti).

	Mg	Al	B
MgB_2	0.3814	-	3.8093
AlB_2	-	0.8703	4.0649
$Mg_{0.5}Al_{0.5}B_2$	0.3784	0.7988	3.9557
$Mg_{0.5}Al_{0.5}B_2$(anti)	0.3653	0.9428	3.92295
$Mg_{1-x}Al_xB_2$(A)	0.3722	1.2722	3.8258
$Mg_{1-x}Al_xB_2$(B)	0.3364	0.00	3.9988
$Mg_{1-x}Al_xB_2$(C)	0. 3329	0.00	3.9169

Table 11: The effective Mg, Al and B valence charge for MgB_2, AlB_2, $Mg_{0.5}Al_{0.5}B_2$ and $Mg_{0.5}Al_{0.5}B_2$(anti), as obtained from Bader charge decomposition. The $Mg_{1-x}Al_xB_2$(A) , $Mg_{1-x}Al_xB_2$(B) , $Mg_{1-x}Al_xB_2$(C) numbers refer to averages over all atoms. The corresponding numbers for individual atoms are summarized in Table 12.

	B1	B2	B3	B4
$Mg_{1-x}Al_xB_2$(A)	3.8286	3.8438	3.8641	3.8641
$Mg_{1-x}Al_xB_2$(B)	3.8445	4.0652	4.1646	4.1796
$Mg_{1-x}Al_xB_2$(C)	3.78875	3.7915	3.85495	3.84905

Table 12: The effective B valence charge for individual atoms in $Mg_{1-x}Al_xB_2$(A) , $Mg_{1-x}Al_xB_2$(B) and $Mg_{1-x}Al_xB_2$(C). B1 is in the middle of the MgB_2 marix, B2 on the MgB_2 side of the $MgB_2/AlB_2/Mg_{0.5}Al_{0.5}B_2$ interface, B3 on the $AlB_2/Mg_{0.5}Al_{0.5}B_2$ side of the $MgB_2/AlB_2/Mg_{0.5}Al_{0.5}B_2$ interface and B4 in the middle of the $AlB_2/Mg_{0.5}Al_{0.5}B_2$ domain, see also Figs. 18, 19 and 20.

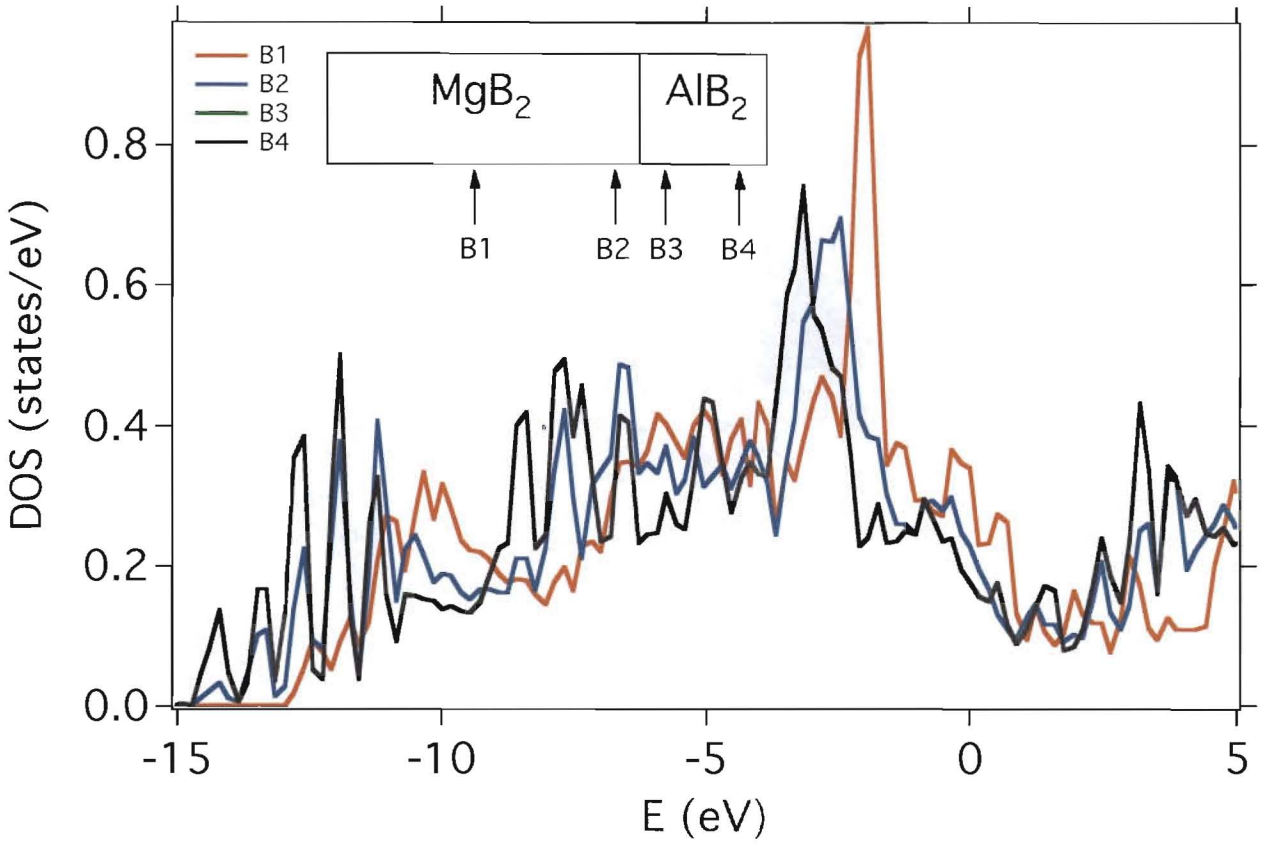

Figure 18: B projected density of states (PDOS) for $Mg_{0.75}Al_{0.25}B_2$(A). The position of the B atoms relative the phase boundary is illustrated in the inset. Note that the B3 and B4 PDOS overlap, since these sites are equivalent due to the small extension of the AlB_2 domain.

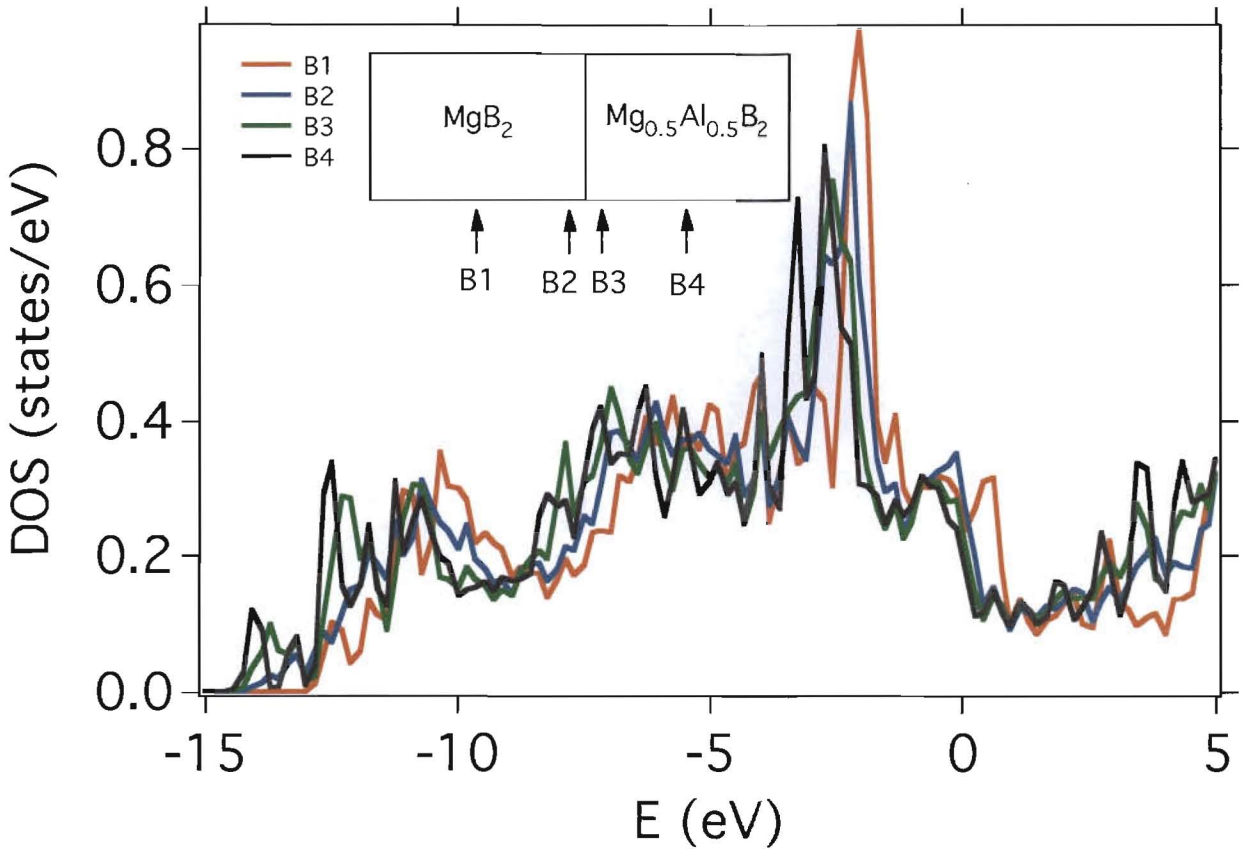

Figure 19: B projected density of states (PDOS) for $Mg_{0.75}Al_{0.25}B_2$(B). The position of the B atoms relative the phase boundary is illustrated in the inset.

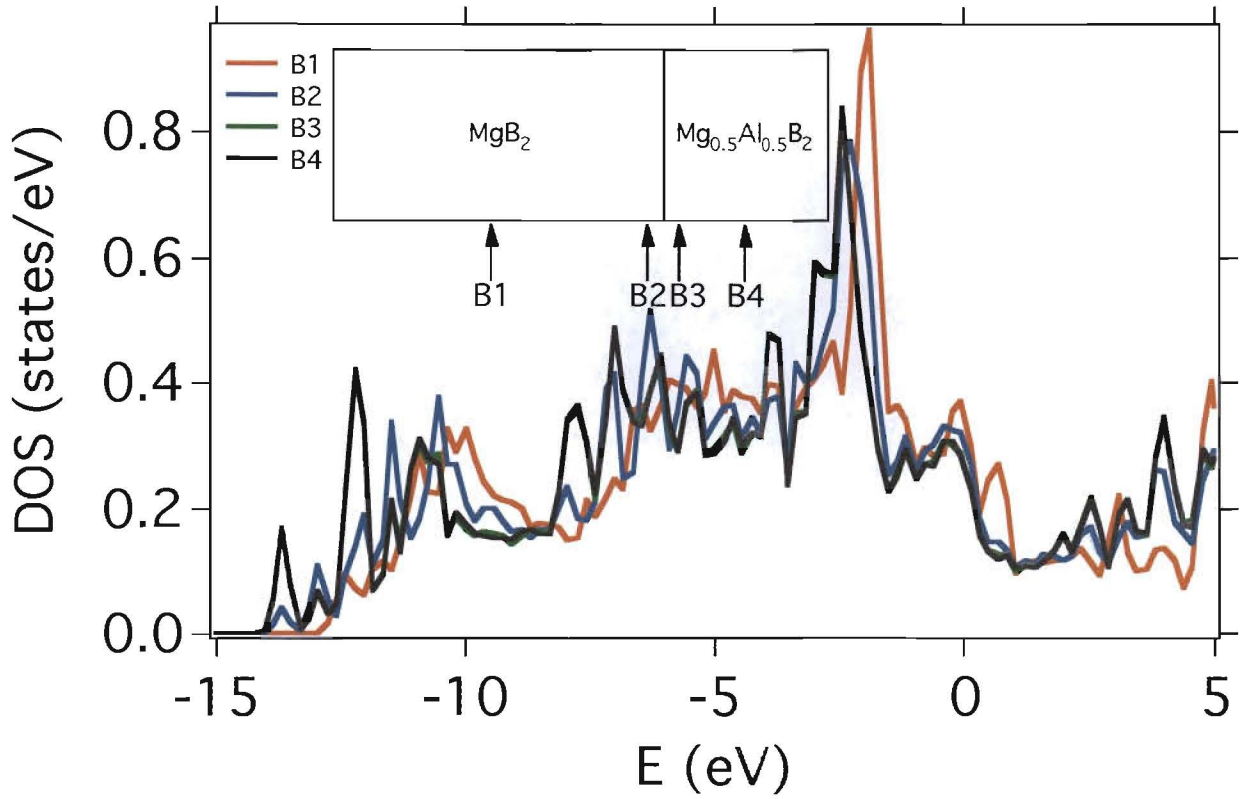

Figure 20: B projected density of states (PDOS) for $Mg_{0.875}Al_{0.125}B_2$(C). The position of the B atoms relative the phase boundary is illustrated in the inset.

Conclusions

In this work we have studied MgB_2-AlB_2 solid solutions that contain nano-scale structure domains of different size, geometry and composition. This system serves as a model case for the concept of nano-scale heterogeneities, which is essential for the understanding of a range of complex materials, e.g. high-T_c superconductors, actinide oxides and actinide alloys. First appropriate Mg-Al-B MEAM potentials were derived and validated using density functional theory calculations. These potentials were then used to study the stability and structure of various $Mg_{1-x}Al_xB_2$ compounds. From the relaxed geometries we simulated the (powder) diffraction patterns by Fourier transforming the atomic pair correlation function. At low temperature the equilibrium phase diagram is comprised of MgB_2+$Mg_{0.5}Al_{0.5}B_2$ two-phase mixtures. The stability of the various nano-scale structure patterns correlates with the size of the coherent Al domains and the stability is further increased by separating

the Al domains into every second metal plane, thus mimicking the $Mg_{0.5}Al_{0.5}B_2$ ordering pattern. Monte Carlo simulations confirm the low temperature MgB_2+$Mg_{0.5}Al_{0.5}B_2$ phase diagram, while disordering starts to take place above 500 K for low Al concentrations and eventually the $Mg_{1-x}Al_xB_2$+$Mg_{0.5}Al_{0.5}B_2$ phase field develops. The simulated diffraction spectra suggest that only semi-infinite AlB_2/$Mg_{0.5}Al_{0.5}B_2$ domains exhibit clear two-phase character, which is associated with the ability of such structures to relax the c lattice parameter according to the optimal Al-B distance in $Mg_{0.5}Al_{0.5}B_2$/AlB_2. Al domains of finite size exhibit some peak splits above a critical size and total Al concentration, but they lack obvious signatures of two separate phases, at least within the range of domain sizes that we were able to investigate in the present work. Mixed Al/Mg domains reveal properties that are almost identical to random solid solutions. Density functional theory calculations were used to study how heterogeneous structure domains influence the electronic properties, i.e. the local charge distribution, and we identified unique features of the B orbitals that belong to the $Mg_{0.5}Al_{0.5}B_2$/AlB_2 domains.

References

1. J. Nagamatsu, N. Nakagawa, T. Muranaka, Y. Zenitani and J. Akimitsu, Nature **410**, 63 (2001).

2. H. J. Choi, M. L. Cohen and S. G. Louie, Phys. Rev. B **73**, 104520 (2006).

3. S. Margadonna, K. Prassides, I. Arvanitidis, M. Pissas, G. Papavassiliou and A. N. Fitch, Phys. Rev. B **66**, 014518 (2002).

4. S. L. Bud'ko, G. Lapertot, C. Petrovic, C. E. Cunningham, N. Anderson and P. C. Canfield, Phys. Rev. Lett. **86**, 1877 (2001).

5. D.G. Hinks, H. Claus, and J. D. Jorgensen, Nature **411**, 457 (2001).

6. G. Karapetrov, M. Iavarone, W. K. Kwok, G. W. Crabtree and D. G. Hinks, Phys. Rev. Lett. **86**, 4374 (2001).

7. B. Lorenz, R. L. Meng, and C. W. Chu, Phys. Rev. B **64**, 012507 (2001).

8. E. Saito, T. Takenobu, T. Ito, Y. Iwasa, K. Prassides and T. Arima, J. Phys.: Condens. Matter **13**, L267 (2001).

9. S. Margadonna, T. Muranaka, K. Prassides, I. Maurin, K. Brigatti, R.M. Ibberson, M. Arai, M. Takata and J. Akimitsu, J. Phys.: Condens. Matter **13**, L795 (2001).

10. 3. H. J. Choi, D. R., H. S., M. L. Cohen, S. G. Louie, Nature **418**, 758 (2002).

11. J. S. Slusky, N. Rogado, K. A. Regan, M. A. Hayward, P. Khalifah, T. He, K. Inumaru, S. M. Loureiro, M. K. Haas, H. W. Zandbergen and R. J. Cava, Nature **410**, 343 (2001).

12. Y. G. Zao, X. P. Zhang, P. T. Qiao, H. T. Zhang, S. L. Jian, B. S. Cao, M. H. Zhu, Z. H. Han, X. L. Wang, and B. L. Gu, Physica C **361**, 91 (2001).

13. T. Takenobu, T. Ito, D. H. Chi, K. Prassides and Y. Iwasa, Phys. Rev. B **64**, 134513 (2001).

14. I. Maurin, S. Margadonna, K. Prassides, T. Takenobu, T. Ito, D. H. Chi, Y. Iwasa, and A. Fitch, Physica B **318**, 392 (2002).

15. J .M. An and W. E. Pickett, Phys. Rev. Lett. **86**, 4366 (2001).

16. 8. B. Renker, K. B. Bohnen, R. Heid, D. Ernst, H. Schober, M. Koza, P. Adelmann, P. Schweiss, and T. Wolf, Phys. Rev. Lett. **88**, 067001 (2002).

17. J. Q. Li, L. Li, F. M. Liu, C. Dong, J. Y. Xiang, and Z. X. Zhao, Phys. Rev. B **65**, 132505 (2002).

18. R. J. Cava , H. W. Zandbergen, K. Inumaru, Physica C **385**, 8 (2003).

19. P. Postorino, A. Congeduti, P. Dore, A. Nucara, A. Bianconi, D. Di Castro, S. De Negri, and A. Saccone, Phys. Rev. B **65**, 020507 (2001).

20. Z. A. Xu, N. P. Ong, Y. Wang, T. Kakeshita and S. Uchida, Nature **406**, 486 (2000).

21. J. Zaanen, Nature **404**, 714 (2000).

22. J. M. Tranquada, B. J. Sternlieb, J. D. Axe, Y. Nakamura and S. Uchida, Nature **375**, 561 (1995).

23. J. M. Tranquada, K. Nakajima, M. Braden, L. Pintschovius, R. J. McQueeney, Phys. Rev. Lett **88**, 755051 (2002).

24. A. Cho, Science **295**, 1992 **(2002)**.

25. A. Moreo, S. Yunoki, E and Dagotto, Science **283**, 2034 (1999).

26. E. Dagotto, T. Hotta and A. Moreo, Phys. Rep. **344**, 1 (2001).

27. S. D. Conradson, B. D. Begg, D. L. Clark, C. Den Auwer, F. J. Espinosa- Faller, P. L. Gordon, N. J. Hess, R. Hess, D. W. Keogh, L. A. Morales, M. P. Neu, W. Runde, C. D. Tait, D. K. Veirs and P. M. Villella, Inorg. Chem. **42**, 3715 (2003).

28. S. D. Conradson, B. D. Begg, D. L. Clark, C. den Auwer, M. Ding, P. K. Dorhout, F. J. Espinosa-Faller, P. L. Gordon, R. G. Haire and N. J. Hess, J. Am. Chem. Soc. **126**, 13443 (2004).

29. To be published.

30. R. C. Howell, S. D. Conradson and A. J. Garcia-Adeva, J. Phys. Chem. B **111**, 159 (2007).

31. A. J. Garcia-Adeva, R. C. Howell, S. D. Conradson, J. F. M. de Leon, F. J. Espinosa-Faller, *et al.* J. Phys. Chem. B **109**, 10419 (2005).

32. F. J Espinosa-Faller, R. C. Howell, A. J. Garcia-Adeva, S. D. Conradson and A. Y. Ignatov, *et al.* J. Phys. Chem. B **109**, 10406 (2005).

33. J. M. Osorio-Guillen, S. I. Simak, Y. Wang, B. Johansson and R. Ahuja, Solid State Communications **123**, 257 (2002).

34. M. I. Baskes, Phys. Rev. B **46**, 2727 (1992).

35. M. I. Baskes, J. E. Angelo, C. L. Bisson, Modell. Simul. Mater. Sci. Eng. **2**, 505 (1994).

36. M. I. Baskes, Mater. Chem. Phys. **50**, 152 (1997).

37. M. I. Baskes, Phys. Rev. Lett. **59**, 2666 (1987).

38. M. I. Baskes, J. S. Nelson and A. F. Wright , Phys. Rev. B **40**, 6085 (1989).

39. M. I. Baskes, Phys. Rev. B **46**, 2727 (1992).

40. M. I. Baskes and R. A. Johnson, Modell. Simul. Mater. Sci. Eng **2**, 147 (1994).

41. J. H. Rose, J. R. Smith, F. Guinea and J. Ferrante, Phys. Rev. B **29**, 2963 (1984).

42. M. I. Baskes, Mater. Sci. Eng., A **261**, 165 (1999).

43. B. Jelinek, J. Houze, K. Sungho, M. F. Horstemeyer, M. I Baskes and S.-G. Kim, Phys. Rev. B **75**, 054106 (2007).

44. G. Kresse and J. Hafner, Phys. Rev. B **48**, 13115 (1993).

45. G. Kresse and J. Furthmüller, Comp. Mater. Sci. **6**, 15 (1996).

46. G. Kresse and J. Furthmüller, Phys. Rev. B **54**, 11169 (1996).

47. G. Kresse and D. Joubert, Phys. Rev. B **59**, 1758 (1999).

48. P. E. Blöchl, Phys. Rev. B **50**, 17953 (1994).

49. J. P. Perdew, K. Burke and M. Ernzerhof. Phys. Rev. Lett. **77**, 3865 (1996).

50. J. P. Perdew, K. Burke and M. Ernzerhof. Phys. Rev. Lett., **78**, 1396 (1997).

51. M. Methfessel and A. Paxton, Phys. Rev. B **40**, 3616 (1989).

52. F. D. Murnaghan, Proc. Natl. Acad. Sci. U.S.A **30**, 244 (1944).

53. ``First-principles calculation of Elastic Properties", in *Intermetallic Compounds: Vol. 1, Principles,*

J. H. Westbrook and R. L. Fleischer, eds. (Wiley, London: 1994).

54. G. Henkelman, A. Arnaldsson, J. Jonsson, Comp. Mat. Sci. **36**, 354 (2006).

55. R. C. Howell, T. Proffen, S. D. Conradson, Phys. Rev. B **73**, 094107 (2006).

56. G. Wang, M. A. Van Hove, P. N. Ross, M. I. Baskes, J. Chem. Phys. **122,** 1 (2005).

57. P. Ravindran, P. Vajeeston, R. Vidya, A. Kjekshus and H. Fjellvåg, Phys. Rev. B **64**, 224509.

58. P. Souvatzis , J. M. Osorio-Guillen, R. Ahuja, A. Grechnev and O. Eriksson, J. Phys. Condens. Matter **16,** 5241 (2004).

59. Zhou Xiao-Lin, Liu Ke, Chen Xiang-Rong and Zhu Jun, Chinese Phys. **15** 3014 (2006).

60. J. L. Hoard, R. E. Hughes, D. E. Sands, Journal of the American Chemical Society **80**, 4507 (1958).

61. To be published.

62. T. Vogt, G. Schneider, J.A. Hriljac, G. Yang, J.S. Abell, Phys. Rev. B **63** 220505(R) (2001).

63. I. I. Mazin and V. P. Antropov, Physica C **385**, 49 (2003).

64. I. Loa, K. Kunc, K. Syassen and P. Bouvier Phys. Rev. B **66**, 134101 (2002).

65. H. W. Zandbergen, M. Y. Wu, M. A. Hayward, M. K. Haas, R. J. Cava, Physica C **366**, 221 (2002).